bioRxiv preprint doi: https://doi.org/10.1101/2021.12.14.472513; this version posted December 15, 2021. The copyright holder for this preprint (which was not certified by peer review) is the author/funder, who has granted bioRxiv a license to display the preprint in perpetuity. It is made available under aCC-BY-NC-ND 4.0 International license.

# Metalloproteinase-dependent and TMPRSS2-independnt cell surface entry pathway of SARS-CoV-2 requires the furin-cleavage site and the S2 domain of spike protein

**Mizuki Yamamoto[1], Jin Gohda[1], Ayako Kobayashi[1], Keiko Tomita[1], Youko Hirayama[1], Naohiko Koshikawa[2], Motoharu Seiki[3], Kentaro Semba[4], Tetsu Akiyama[5], Yasushi Kawaguchi[1,6] and Jun-ichiro Inoue[7*]**

[1]Research Center for Asian Infectious Diseases, The Institute of Medical Science, The University of Tokyo, Tokyo 108-8639, Japan

[2]Department of Life Science and Technology, Tokyo Institute of Technology, Yokohama 226-8501 Japan

[3]Division of Cancer Cell Research, The Institute of Medical Science, The University of Tokyo, Tokyo 108-8639, Japan

[4]Department of Life Science and Medical Bio-Science, Waseda University, Shinjuku-ku, Tokyo, 162-8480, Japan

[5]Laboratory of Molecular and Genetic Information, Institute for Quantitative Biosciences, The University of Tokyo, Tokyo 113-0032, Japan

[6]Division of Molecular Virology, Department of Microbiology and Immunology, The Institute of Medical Science, The University of Tokyo, Tokyo 108-8639, Japan

[7]Research Platform Office, The Institute of Medical Science, The University of Tokyo, Tokyo 108-8639, Japan

* Corresponding author:

E-mail: jun-i@ims.u-tokyo.ac.jp (JI)

bioRxiv preprint doi: https://doi.org/10.1101/2021.12.14.472513; this version posted December 15, 2021. The copyright holder for this preprint (which was not certified by peer review) is the author/funder, who has granted bioRxiv a license to display the preprint in perpetuity. It is made available under aCC-BY-NC-ND 4.0 International license.

**Abstract**

The ongoing global vaccination program to prevent SARS-CoV-2 infection, the causative agent of COVID-19, has had significant success. However, recently virus variants have emerged that can evade the immunity in a host achieved through vaccination. Consequently, new therapeutic agents that can efficiently prevent infection from these new variants, and hence COVID-19 spread are urgently required. To achieve this, extensive characterization of virus-host cell interactions to identify effective therapeutic targets is warranted. Here, we report a cell surface entry pathway of SARS-CoV-2 that exists in a cell type-dependent manner is TMPRSS2-independent but sensitive to various broad-spectrum metalloproteinase inhibitors such as marimastat and prinomastat. Experiments with selective metalloproteinase inhibitors and gene-specific siRNAs revealed that a disintegrin and metalloproteinase 10 (ADAM10) is partially involved in the metalloproteinase pathway. Consistent with our finding that the pathway is unique to SARS-CoV-2 among highly pathogenic human coronaviruses, both the furin cleavage motif in the S1/S2 boundary and the S2 domain of SARS-CoV-2 spike protein are essential for metalloproteinase-dependent entry. In contrast, the two elements of SARS-CoV-2 independently contributed to TMPRSS2-dependent S2 priming. The metalloproteinase pathway is involved in SARS-CoV-2-induced syncytia formation and

bioRxiv preprint doi: https://doi.org/10.1101/2021.12.14.472513; this version posted December 15, 2021. The copyright holder for this preprint (which was not certified by peer review) is the author/funder, who has granted bioRxiv a license to display the preprint in perpetuity. It is made available under aCC-BY-NC-ND 4.0 International license.

cytopathicity, leading us to theorize that it is also involved in the rapid spread of SARS-CoV-2 and the pathogenesis of COVID-19. Thus, targeting the metalloproteinase pathway in addition to the TMPRSS2 and endosome pathways could be an effective strategy by which to cure COVID-19 in the future.

## Author Summary

To develop effective therapeutics against COVID-19, it is necessary to elucidate in detail the infection mechanism of the causative agent, SARS-CoV-2, including recently emerging variants. SARS-CoV-2 binds to the cell surface receptor ACE2 via the Spike protein, and then the Spike protein is cleaved by host proteases to enable entry. Selection of target cells by expression of these tissue-specific proteases contributes to pathogenesis. Here, we found that the metalloproteinase-mediated pathway is important for SARS-CoV-2 infection, variants included. This pathway requires both the prior cleavage of Spike into two domains and a specific sequence in the second domain S2, conditions met by SARS-CoV-2 but lacking in the related human coronavirus SARS-CoV. The contribution of several proteases, including metalloproteinases, to SARS-CoV-2 infection was cell type dependent, especially in cells derived from kidney, ovary, and endometrium, in which SARS-CoV-2 infection was metalloproteinase-dependent. In

bioRxiv preprint doi: https://doi.org/10.1101/2021.12.14.472513; this version posted December 15, 2021. The copyright holder for this preprint (which was not certified by peer review) is the author/funder, who has granted bioRxiv a license to display the preprint in perpetuity. It is made available under aCC-BY-NC-ND 4.0 International license.

these cells, inhibition of metalloproteinases by treatment with marimastat or prinomastat, whose safety was previously confirmed in clinical trials, was important in preventing cell death. Our study provides new insights into the complex pathogenesis unique to COVID-19 and relevant to the development of effective therapies.

bioRxiv preprint doi: https://doi.org/10.1101/2021.12.14.472513; this version posted December 15, 2021. The copyright holder for this preprint (which was not certified by peer review) is the author/funder, who has granted bioRxiv a license to display the preprint in perpetuity. It is made available under aCC-BY-NC-ND 4.0 International license.

## Introduction

Severe acute respiratory syndrome coronavirus 2 (SARS-CoV-2), the causative agent of coronavirus disease 2019 (COVID-19), was first recognized in late 2019 and led to the development of a global pandemic in 2020[1]. Two other human coronaviruses, SARS-CoV[2, 3] and Middle East respiratory syndrome coronavirus (MERS-CoV)[4], are also capable of inducing lethal pneumonia and systemic symptoms. However, SARS-COV-2 has been found to also exhibit enhanced pathogenicity and transmissibility[5, 6]. Effective vaccines have been developed, and ongoing global vaccination programs have significantly curbed the spread of infection[7, 8]. However, current vaccinations may provide imperfect protection as new variants of the virus that can spread more easily and evade the host immunity achieved through vaccination have been reported[7, 9-11]. Furthermore, although several drugs that may provide effective treatments for COVID-19 are currently under clinical trial and awaiting approval[12, 13], it is currently unclear if daily life around the world will ever return to that of pre-COVID-19 times. Consequently, further extensive characterization of the virus and its interactions with host cells are required to develop vaccines and therapeutic agents that efficiently prevent infection from the new emerging highly infective variants so as to limit further worsening of COVID-19.

bioRxiv preprint doi: https://doi.org/10.1101/2021.12.14.472513; this version posted December 15, 2021. The copyright holder for this preprint (which was not certified by peer review) is the author/funder, who has granted bioRxiv a license to display the preprint in perpetuity. It is made available under aCC-BY-NC-ND 4.0 International license.

The initiation of SARS-CoV-2 entry requires two steps after its spike (S) protein is cleaved into S1 and S2 by furin-like proteases expressed in virus-producing cells prior to viral release[14-16]. First, the S protein binds to its receptor angiotensin converting enzyme 2 (ACE2) in the plasma membrane through its receptor-binding domain (RBD)[17, 18]. Second, the S2 protein is cleaved to generate S2′ by either cell surface transmembrane serine protease 2 (TMPRSS2)[19] or endosomal protease cathepsin-B/L[19, 20]. This cleavage is called priming, and exposes the fusion peptide within S2′, allowing it to stick into the plasma or endosomal membrane, resulting in fusion between the viral envelope and the cellular membrane (envelope fusion). This fusion allows viral RNA to enter the cytoplasm where it replicates. Whether SARS-CoV-2 viruses use the plasma membrane, the endosome pathway, or both is dependent on the cell type[19, 21, 22]. Furin-mediated cleavage at the S1/S2 boundary leads to efficient viral entry into airway cells[15, 16], where the TMPRSS2-dependent surface entry route dominates endosomal entry[19, 23].

In this study, we screened for inhibitors of SARS-CoV-2 infection and identified a cell surface entry pathway of SARS-CoV-2 that is TMPRSS2-independent but sensitive to various metalloproteinase inhibitors. Interestingly, the metalloproteinase-dependent pathway requires both the furin cleavage motif in the S1/S2 boundary and the

bioRxiv preprint doi: https://doi.org/10.1101/2021.12.14.472513; this version posted December 15, 2021. The copyright holder for this preprint (which was not certified by peer review) is the author/funder, who has granted bioRxiv a license to display the preprint in perpetuity. It is made available under aCC-BY-NC-ND 4.0 International license.

S2 domain of SARS-CoV-2, which is unique to SARS-CoV-2. These results suggest that co-operation between furin and some metalloproteinases could be crucial for SARS-CoV-2 spread and disease development *in vivo*. Consequently, targeting the metalloproteinase-pathway in addition to the TMPRSS2 and cathepsin-B/L pathways could be an effective strategy to cure COVID-19.

## Results

### TMPRSS2-independent membrane fusion induced by the S protein of SARS-CoV-2 is blocked by metalloproteinase inhibitors

In this investigation, the screening system used to detect effective inhibitors of coronavirus infection included a quantitative cell fusion assay between effector cells expressing S protein and target cells expressing either ACE2 (for SARS-CoV and SARS-CoV-2)[24] or CD26 (for MERS-CoV)[25], with or without TMPRSS2 (S1a,b Fig). Quantitation was accomplished using the dual split chimeric reporter proteins (DSP)1-7 and DSP8-11, which contain both *Renilla* luciferase (RL) and green fluorescent protein (GFP) variants[26]. The DSP assay quantifies the degree of membrane fusion between the effector cells expressing DSP1-7 and the target cells expressing DSP8-11 based on the RL activity (S1c Fig). During analysis with the DSP cell fusion assay, a significant

bioRxiv preprint doi: https://doi.org/10.1101/2021.12.14.472513; this version posted December 15, 2021. The copyright holder for this preprint (which was not certified by peer review) is the author/funder, who has granted bioRxiv a license to display the preprint in perpetuity. It is made available under aCC-BY-NC-ND 4.0 International license.

121 amount of ACE2-dependent but TMPRSS2-independent cell-cell fusion was induced by
122 the S protein of SARS-CoV-2, but not by that of SARS- or MERS-CoV (Fig 1a,b).
123 Consistent with this finding, the cell fusion with TMPRSS2 in the target cells induced by
124 the S protein of SARS-CoV and MERS-CoV was completely blocked when TMPRSS2
125 was inhibited with 1 μM nafamostat, while approximately 20% of the fusion by the
126 SARS-CoV-2 S protein remained, even in the presence of 10 μM nafamostat (Fig 1c).
127 This amount of residual fusion was almost equal to that induced by the SARS-CoV-2 S
128 protein in the absence of TMPRSS2 (Fig 1d).

129 To explore the mechanism of TMPRSS2-independent membrane fusion, we
130 screened the Validated Compound Library (1,630 clinically approved compounds and
131 1,885 pharmacologically active compounds) obtained from the Drug Discovery Initiative
132 (The University of Tokyo). We aimed to identify compounds that preferentially inhibited
133 SARS-CoV-2 S protein-induced TMPRSS2-independent fusion and not TMPRSS2-
134 dependent fusion. We compared the relative fusion values of the target cells expressing
135 both TMPRSS2 and ACE2 (X-axis of Fig 2a) with those of the target cells expressing
136 ACE2 alone (Y-axis of Fig 2a), and chose for further validation compounds that limited
137 the fusion without TMPRSS2 by less than 60% and allowed the fusion with TMPRSS2
138 by more than 70% (Fig 2a). The compounds selected included two metalloproteinase

bioRxiv preprint doi: https://doi.org/10.1101/2021.12.14.472513; this version posted December 15, 2021. The copyright holder for this preprint (which was not certified by peer review) is the author/funder, who has granted bioRxiv a license to display the preprint in perpetuity. It is made available under aCC-BY-NC-ND 4.0 International license.

inhibitors (ilomastat, CTS-1027), three tyrosine kinase inhibitors (sunitinib, PD-166285, PD-173952), two checkpoint kinase inhibitors (PF-477736, AZD-7762), a protein kinase C inhibitor (midostaurin), and a hormonal contraceptive (algestone). Ilomastat and CTS-1027 preferentially inhibited the TMPRSS2-independent fusion in a dose-dependent manner without affecting TMPRSS2-dependent fusion (Fig 2b). Furthermore, the luciferase activities of the preformed DSP1-7/DSP8-11 complex were not affected, confirming the specificity of the DSP assay (S2a,b Fig). However, other compounds inhibited both the TMPRSS2-dependent and -independent fusions to similar degrees (S3 Fig). These data suggest that the metalloproteinase-dependent cell surface entry pathway (the metalloproteinase pathway) may be unique to SARS-CoV-2 among human pathogenic coronaviruses with high mortality rates. Considering that metalloproteinase inhibitors could thus possibly be used as prophylactic or therapeutic agents for COVID-19, we further demonstrated that marimastat[27] and prinomastat[28] (whose safety was previously confirmed in clinical trials to investigate their use as anticancer agents, such as CTS-1027[29]) can preferentially block the TMPRSS2-independent fusion induced by the SARS-CoV-2 S protein (Fig 2b and S2b Fig).

**The metalloproteinase pathway is SARS-CoV-2 specific and cell type-dependent**

bioRxiv preprint doi: https://doi.org/10.1101/2021.12.14.472513; this version posted December 15, 2021. The copyright holder for this preprint (which was not certified by peer review) is the author/funder, who has granted bioRxiv a license to display the preprint in perpetuity. It is made available under aCC-BY-NC-ND 4.0 International license.

We investigated whether the metalloproteinase pathway exists in SARS-CoV-2 S-bearing vesicular stomatitis virus (VSV) pseudovirus. The pseudovirus entry into the A704 cells (human kidney) was entirely blocked by 1 μM marimastat (Fig 3a). This indicates that the metalloproteinase pathway is involved in the entry of the virus, and that 1 μM marimastat could be used to determine if the pathway exists in other cells. Similarly, all entry pathways in OVISE cells (human ovary) were blocked by 25 μM E-64d (Fig 3a), indicating that it could be used to investigate the existence of cathepsin-B/L-dependent endosome pathways in other cells. Furthermore, the entry pathways in Calu-3 cells (human lung) were entirely blocked by 0.1 μM nafamostat (Fig 3a), which indicates that more than 0.1 μM nafamostat may be used to investigate the existence of the TMPRSS2-dependent surface entry pathways in other cells. Consequently, 1 μM marimastat, 25 μM E-64d, and 10 μM nafamostat were used to elucidate the patterns of the entry pathways in various cells. Marimastat significantly inhibited the pseudovirus entry into VeroE6 (African green monkey kidney), HEC50B (human endometrium), OVTOKO (human ovary), and A704 cells (Fig 3b). In addition to the metalloproteinase pathway, virus entry was partially inhibited by E-64d, and the combination of marimastat and E-64d showed additive effects in VeroE6, HEC50B, and OVTOKO cells (Fig 3b). These results suggest that the metalloproteinase and endosomal pathways are mutually independent. Neither

bioRxiv preprint doi: https://doi.org/10.1101/2021.12.14.472513; this version posted December 15, 2021. The copyright holder for this preprint (which was not certified by peer review) is the author/funder, who has granted bioRxiv a license to display the preprint in perpetuity. It is made available under aCC-BY-NC-ND 4.0 International license.

175 marimastat nor nafamostat alone significantly inhibited the entry pathways of IGROV1
176 (human ovary), OUMS-23 (human colon), or OVISE, whereas E-64d significantly
177 inhibited the entry pathways of IGROV1 and OUMS-23 cells and the overall entry
178 pathway into the OVISE cells (Fig 3c). Interestingly, E-64d resistant entry in IGROV1
179 cells was inhibited by the combination of marimastat with E-64d while the E-64d resistant
180 entry into OUMS-23 cells was inhibited by the combination of nafamostat and E-64d.
181 These results indicate that the endosome entry pathway dominates these cells, while
182 coexisting with either the metalloproteinase or TMPRSS2 surface pathway. Nafamostat
183 inhibited the overall entry pathways into the Calu-3 and Caco-2 (human colon) cells,
184 while marimastat and E-64d showed no inhibitory effects. (Fig 3d). Together, these
185 findings show that the metalloproteinase-dependent cell surface entry pathway exists in
186 a cell type-dependent manner and coexists with the endosome pathway in some cell lines.
187 As we could not find cell lines with both metalloproteinase- and TMPRSS2-dependent
188 cell surface entry pathways, we generated HEC50B cell lines ectopically expressing
189 TMPRSS2 (HEC50B-TMPRSS2). In the HEC50B-TMPRSS2 cells, approximately 80%
190 of the entry pathways were TMPRSS2-dependent, while the rest were predominantly
191 metalloproteinase-dependent (Fig 3e). This indicates that the metalloproteinase pathway

bioRxiv preprint doi: https://doi.org/10.1101/2021.12.14.472513; this version posted December 15, 2021. The copyright holder for this preprint (which was not certified by peer review) is the author/funder, who has granted bioRxiv a license to display the preprint in perpetuity. It is made available under aCC-BY-NC-ND 4.0 International license.

192 independently coexists with the TMPRSS2 dependent pathway. These results also
193 suggest that there could be cells *in vivo* that naturally have both surface entry pathways.
194
195 **The metalloproteinase pathway requires both the furin-cleavage site and S2 region**
196 **of the SARS-CoV-2 S protein**
197 Our results showed that metalloproteinase-dependent and TMPRSS2-independent cell-
198 cell fusion was induced by the S protein of SARS-CoV-2 but not by that of SARS-CoV
199 or MERS-CoV (Fig 1a,b). In line with these results, metalloproteinase-dependent entry
200 was observed only when the pseudovirus bearing the S protein of SARS-CoV-2, but not
201 SARS-CoV or MERS-CoV, was used in HEC50B (Fig 4a), A704 (S4a Fig), and VeroE6
202 cells (S4b Fig). Furthermore, pseudoviruses bearing the S protein of HCoV-NL63 and
203 WIV1-CoV, which like SARS-CoV-2 use ACE2 as their receptor, cannot utilize the
204 metalloproteinase pathway in HEC50B cells (Fig 4b). While SARS-CoV-2 S uses both
205 the metalloproteinase and endosome pathways, SARS-CoV, MERS-CoV, HCoV-NL63,
206 and WIV1-CoV S exclusively use the endosome pathway, and none of these S proteins
207 can use the metalloproteinase or TMPRSS2 pathway in HEC50B (Fig 4a,b), A704 (S4a
208 Fig), and VeroE6 cells (S4b Fig). The ability to use the metalloproteinase pathway and

bioRxiv preprint doi: https://doi.org/10.1101/2021.12.14.472513; this version posted December 15, 2021. The copyright holder for this preprint (which was not certified by peer review) is the author/funder, who has granted bioRxiv a license to display the preprint in perpetuity. It is made available under aCC-BY-NC-ND 4.0 International license.

sensitivities against various protease inhibitors are conserved among the variants of SARS-CoV-2 we tested (S5 Fig).

The S proteins of SARS-CoV-2 and MERS-CoV have furin cleavage sites (Arg-X-X-Arg) in their S1/S2 boundary area, and they were efficiently cleaved during the preparation of the pseudovirus (Fig 4c,d). In contrast, the S proteins of SARS-CoV, HCoV-NL63, and WIV1-CoV, which do not use the metalloproteinase pathway, do not have furin cleavage site and are not cleaved to any notable degree (Fig 4c,d and S6 Fig). Given that the MERS-CoV S protein does not use the metalloproteinase pathway (Fig 4a) even though it harbors a furin cleavage site and was efficiently cleaved, we speculated that furin-catalyzed S protein cleavage is a prerequisite but not sufficient for using the metalloproteinase pathway. To test this hypothesis, we generated pseudoviruses bearing chimeric S proteins in which the S1, S1/S2 boundary, and S2 domains were derived from either SARS-CoV or SARS-CoV-2 (Fig 4c,d). As expected, the S2 fragment of the C-terminal Flag-tagged S protein was mainly detected with anti-Flag antibody when pseudoviruses bearing S proteins with the furin-cleavage site (S121, S122, SARS-CoV-2 S (222), and S221) were analyzed (Fig 4d). In contrast, uncleaved S protein (S0) was mainly detected when S proteins without the furin-cleavage site (SARS-CoV S (111), S112, S212, and S211) were used (Fig 4d). When only section, the S1/S2 boundary or the

bioRxiv preprint doi: https://doi.org/10.1101/2021.12.14.472513; this version posted December 15, 2021. The copyright holder for this preprint (which was not certified by peer review) is the author/funder, who has granted bioRxiv a license to display the preprint in perpetuity. It is made available under aCC-BY-NC-ND 4.0 International license.

S2 domain, was replaced with the corresponding domain of SARS-CoV-2 in the SARS-CoV S protein (S121, S112), the metalloproteinase pathway did not appear (Fig 4e). However, when both the S1/S2 and S2 domains were replaced with the corresponding domains of SARS-CoV-2 (S122), the metalloproteinase pathway appeared in addition to the endosome pathway (Fig 4e), similar to the pattern observed for bona fide SARS-CoV-2 S (S222) (Fig 4f). Furthermore, when either the S1/S2 or S2 domain was replaced with the corresponding domain of SARS-CoV in the SARS-CoV-2 S protein (S212, S221), the metalloproteinase pathway disappeared (Fig 4f). Similar requirements for the S1/S2 boundary and S2 domains for SARS-CoV-2 to use the metalloproteinase pathway were also observed in VeroE6 cells (S4c,d Fig). These results indicate that both the S1/S2 boundary and S2 domain of SARS-CoV-2 are strictly required for the virus to utilize the metalloproteinase pathway when the endosome pathway coexists.

To compare the structural requirements needed for the S protein to use the metalloproteinase pathway with those needed to use the TMPRSS2 pathway in cells with the endosome pathway as an alternative, we used HEC50B-TMPRSS2 and VeroE6 cells ectopically expressing TMPRSS2 (VeroE6-TMPRSS2). While both these cell types exhibit the TMPRSS2 and endosome pathways depending on the source of S protein (Fig 4g and S4e Fig), HEC50B-TMPRSS2 cells in addition maintained a significant amount

bioRxiv preprint doi: https://doi.org/10.1101/2021.12.14.472513; this version posted December 15, 2021. The copyright holder for this preprint (which was not certified by peer review) is the author/funder, who has granted bioRxiv a license to display the preprint in perpetuity. It is made available under aCC-BY-NC-ND 4.0 International license.

of the metalloproteinase pathway (approximately 20% of the total entry pathway) (Fig 3e), whereas most of the metalloproteinase pathway disappeared in the VeroE6-TMPRSS2 cells when compared with their parental line (Fig 3b and S4e Fig). Given that the metalloproteinase pathway is dependent on the structural features of the S protein, its blockade by marimastat will promote protein structural requirements for S protein to use the TMPRSS2 pathway in HEC50B-TMPRSS2 (Fig 4g-i) but not in VeroE6-TMPRSS2 cells (S4e-g Fig). In both cell types, SARS-CoV-2 predominantly used the TMPRSS2 entry pathway, while SARS-CoV used the endosome pathway (Fig 4g and S4e Fig). However, nafamostat partially, but more efficiently, inhibited the entry of S112 and S121 pseudoviruses when compared with SARS-CoV (S111), while it inhibited S122 virus entry almost completely (Fig 4h and S4f Fig). Furthermore, when compared with SARS-CoV-2 (S222), nafamostat only partially inhibited S221 or S212 virus entry, while it scarcely inhibited S211 virus entry (Fig 4i and S4g Fig). These results indicate that the S1/S2 boundary and S2 domain of SARS-CoV-2 additively contribute to the ability of the virus to use the TMPRSS2 pathway. Together, these results show that although both the TMPRSS2 and the metalloproteinase pathways undergo priming of the S protein at the cell surface, the structural requirements of the S protein for efficient priming differ between the metalloproteinase and TMPRSS2 pathways.

bioRxiv preprint doi: https://doi.org/10.1101/2021.12.14.472513; this version posted December 15, 2021. The copyright holder for this preprint (which was not certified by peer review) is the author/funder, who has granted bioRxiv a license to display the preprint in perpetuity. It is made available under aCC-BY-NC-ND 4.0 International license.

**Possible involvement of ADAM-10 in the metalloproteinase-dependent entry of SARS-CoV-2**

In addition to marimastat, other metalloproteinase inhibitors, including prinomastat, ilomastat, and CTS-1027, which block the TMPRSS2-independent cell-cell fusion induced by SARS-CoV-2 S (Fig 2b), inhibited the metalloproteinase-dependent entry of SARS-CoV-2 pseudovirus in VeroE6, HEC50B, and A704 cells (Fig 5a). Since these inhibitors exhibited broad specificity[30-33], selective inhibitors were then used to narrow down the metalloproteinases involved in the metalloproteinase-dependent entry pathway. The VeroE6 and HEC50B cells had significantly E-64d sensitive endosome pathways but the A704 cells did not (Fig 3b). Consequently, selective metalloproteinase inhibitors were tested in the presence of E-64d so that the reduction in the metalloproteinase pathway could be easily recognized in VeroE6 and HEC50B cells (Fig 5a). Similar inhibitory patterns were observed in all three cell lines tested (Fig 5a), and their viabilities were not affected by any of the metalloproteinase inhibitors at the concentrations used in the experiment (S7a-d Fig). These results suggest that the metalloproteinases involved in the pathway are likely to be common to all three cell lines. GW280264X[34] (ADAM10/17 inhibitor) and GI1254023X[34, 35] (MMP9/ADAM10

bioRxiv preprint doi: https://doi.org/10.1101/2021.12.14.472513; this version posted December 15, 2021. The copyright holder for this preprint (which was not certified by peer review) is the author/funder, who has granted bioRxiv a license to display the preprint in perpetuity. It is made available under aCC-BY-NC-ND 4.0 International license.

281 inhibitor) significantly inhibited the metalloproteinase pathway, whereas TAPI2[36]
282 (ADAM-17 inhibitor) and BK-1361[37] (ADAM8 inhibitor) did not (Fig 5a). This
283 suggests that ADAM10 may be involved in the ADAM family. MMP408[30]
284 (MMP3/12/13 inhibitor) and MMP2/9 inhibitor I[38] scarcely affected virus entry,
285 whereas UK370106[39] (MMP3/12 inhibitor) and MMP9 inhibitor I[40] were
286 significantly inhibitory (Fig5a), suggesting that MMP3/9/12/13 may not be crucial, but
287 that the unidentified metalloproteinase, which could be inhibited by UK370106 or MMP9
288 inhibitor I, may be involved in the pathway in cooperation with ADAM10. MLN-
289 4760[41] (ACE2 inhibitor) did not inhibit virus entry (Fig 5a), indicating that the catalytic
290 activity of ACE2, to which the S protein directly binds as a receptor, is not involved. To
291 further confirm the involvement of ADAM10 in the metalloproteinase-dependent
292 pathway, ADAM10 was depleted by siRNA in HEC50B cells. Three independent siRNAs
293 effectively suppressed the expression of both the precursor and active forms of ADAM10
294 (Fig 5b). An ADAM10 knockdown significantly inhibited SARS-CoV-2 pseudovirus
295 entry, while the entry of SARS-CoV, MERS-CoV, and VSVG pseudoviruses were not
296 affected (Fig 5c), indicating that ADAM10 plays a role unique to SARS-CoV-2 in viral
297 entry. Furthermore, we examined the effects of the ADAM10 knockdown on the entry
298 pathway patterns by treating siRNA-transfected cells with either E-64d, marimastat, or a

bioRxiv preprint doi: https://doi.org/10.1101/2021.12.14.472513; this version posted December 15, 2021. The copyright holder for this preprint (which was not certified by peer review) is the author/funder, who has granted bioRxiv a license to display the preprint in perpetuity. It is made available under aCC-BY-NC-ND 4.0 International license.

299 combination of both. The combination treatment with E-64d and marimastat led to an
300 additive effect for the single treatments, resulting in the complete inhibition of viral entry
301 in both cells with normal ADAM10 expression and those with reduced ADAM10
302 expression (Fig 5d). These results indicated that E-64d-resistant viral entry is a
303 metalloproteinase-dependent pathway, while marimastat-resistant viral entry is
304 dependent on the endosome pathway. The ADAM10-knockdown significantly inhibited
305 the metalloproteinase pathway (Fig 5e, E64-d treatment）while the ADAM10-knockdown
306 had only a modest effect on the endosome pathway (Fig 5e, marimastat-treatment),
307 indicating that ADAM10 is involved in the metalloproteinase-dependent entry pathway
308 of SARS-CoV-2.

309 Recently, it was reported that ACE2 shedding by ADAM17 promotes SARS-
310 CoV-2 infection[42]. While a CRISPR/Cas9-mediated knockout of ADAM17 enhanced
311 the accumulation of cellular ACE2 in HEC50B cells due to the inhibition of ACE2
312 shedding (S8a Fig), SARS-CoV-2 S pseudovirus entry was increased, and this was
313 probably because of the enhanced binding of virus to the cell surface ACE2 (S8b Fig).
314 However, the patterns of the metalloproteinase and endosome pathways were similar
315 between the wild-type and ADAM17 knockout cells (S8c Fig), suggesting that ADAM17
316 may not be involved in metalloproteinase-dependent virus entry in HEC50B cells.

bioRxiv preprint doi: https://doi.org/10.1101/2021.12.14.472513; this version posted December 15, 2021. The copyright holder for this preprint (which was not certified by peer review) is the author/funder, who has granted bioRxiv a license to display the preprint in perpetuity. It is made available under aCC-BY-NC-ND 4.0 International license.

**The metalloproteinase-dependent entry pathway of authentic SARS-CoV-2 is involved in syncytia formation and cytopathicity**

To confirm the involvement of the metalloproteinase pathway in authentic SARS-CoV-2 entry, we first evaluated the effects of marimastat and prinomastat on the amount of cytoplasmic viral RNA transcribed from the N gene after infection. Both inhibitors significantly suppressed SARS-CoV-2 infection (Fig 6a). The $IC_{50}$ values of the marimastat and prinomastat were 160 nM and 130 nM in HEC50B cells, and 150 nM and 250 nM in the A704 cells, respectively. The $IC_{50}$ value of the marimastat in the VeroE6 cells was 340 nM. Consistent with the results from the pseudoviruses experiments, nafamostat showed a marked inhibitory effect on the Calu-3 cells but not on the HEC50B, A704, or VeroE6 cells (S9a Fig). In contrast, 25 μM E-64d and 10 mM $NH_4Cl$, which inhibits endosome-lysosome system acidification[43], significantly suppressed SARS-CoV-2 infection in the HEC50B, A704, and VeroE6 cells (S9b,c Fig). This indicated that the endosome pathway coexists with the metalloproteinase pathway to contribute to authentic SARS-CoV-2 infection in these cells. Combination treatments with E-64d/marimastat or $NH_4Cl$/marimastat showed much stronger inhibitory effects than the treatment with each drug alone (Fig 6b). Similarly, combination treatments with

bioRxiv preprint doi: https://doi.org/10.1101/2021.12.14.472513; this version posted December 15, 2021. The copyright holder for this preprint (which was not certified by peer review) is the author/funder, who has granted bioRxiv a license to display the preprint in perpetuity. It is made available under aCC-BY-NC-ND 4.0 International license.

335 nafamostat and marimastat or nafamostat and E-64d showed stronger inhibitory effects
336 than the nafamostat treatment alone in the HEC50B-TMPRSS2 cells (Fig 6c).
337 Furthermore, when all three drugs were combined, they had a much stronger inhibitory
338 effect on viral infection when compared with the two-drug combinations (Fig 6c). These
339 results strongly suggest that drugs that block the metalloproteinase pathway are effective
340 for COVID-19 treatment.

341 Next, we examined whether ADAM10 is involved in SARS-CoV-2 infection.
342 GW280264X[34] (ADAM10/17 inhibitor) and GI1254023X[34, 35] (MMP9/ADAM10
343 inhibitor) significantly suppressed SARS-CoV-2 infection, whereas TAPI2[36] (ADAM-
344 17 inhibitor) did not (Fig 6d). Moreover, the ADAM10 knockdown by siRNA suppressed
345 SARS-CoV-2 infection by approximately 40% (Fig 6e), indicating that ADAM10 is
346 partially involved. This effect was smaller than that for the various metalloproteinase
347 inhibitors (Fig 6a,d), suggesting that metalloproteinases other than ADAM10 are also
348 involved in this pathway.

349 The ability of SARS-CoV-2 to form syncytia and induce cytopathicity is thought
350 to be related to its pathogenesis[44, 45]. To determine whether the metalloproteinase-
351 dependent pathway is involved in syncytia formation, we first used HEC50B cells as a
352 representative for cells that predominantly use the metalloproteinase and endosome

bioRxiv preprint doi: https://doi.org/10.1101/2021.12.14.472513; this version posted December 15, 2021. The copyright holder for this preprint (which was not certified by peer review) is the author/funder, who has granted bioRxiv a license to display the preprint in perpetuity. It is made available under aCC-BY-NC-ND 4.0 International license.

353 pathways. Interestingly, the SARS-CoV-2-induced syncytia formation in HEC50B cells
354 24 h after infection was significantly blocked by 500 nM of marimastat and prinomastat
355 but not notably affected by 25 μM E-64d (Fig 6f and S10 Fig). These results indicate that
356 the metalloproteinase-dependent pathway, but not the endosome pathway, is crucial for
357 syncytium formation, although both pathways similarly reduce viral infection (Fig 6b).
358 Given that the metalloproteinases are normally localized at the cell surface, we used
359 HEC50B-TMPRSS2 cells, which have cell surface TMPRSS2 and metalloproteinase
360 pathways, to investigate their involvement in syncytia formation when they coexist. The
361 SARS-CoV-2-induced syncytia formation in the HEC50B-TMPRSS2 cells was not
362 significantly inhibited by marimastat or nafamostat alone, but was clearly inhibited by
363 the combined treatment (Fig 6g). These results suggest that the metalloproteinase and
364 TMPRSS2 pathways cooperate to form syncytia. Next, we addressed the role of the
365 metalloproteinase pathway in SARS-CoV-2-induced cytotoxicity. SARS-CoV-2-induced
366 cytopathicity of HEC50B cells 3 d after infection was not inhibited by either E-64d,
367 marimastat, or prinomastat alone, but was significantly blocked when cells were treated
368 with E-64d in combination with either marimastat or prinomastat (Fig 6h). In addition,
369 SARS-CoV-2-induced cytopathicity of the HEC50B-TMPRSS2 cells was not inhibited
370 by either E-64d, nafamostat, or marimastat alone, but was significantly blocked when

bioRxiv preprint doi: https://doi.org/10.1101/2021.12.14.472513; this version posted December 15, 2021. The copyright holder for this preprint (which was not certified by peer review) is the author/funder, who has granted bioRxiv a license to display the preprint in perpetuity. It is made available under aCC-BY-NC-ND 4.0 International license.

371 cells were treated with a combination of all three drugs (Fig 6i). These results strongly
372 suggest that the inhibition of the metalloproteinase pathway is crucial to block syncytia
373 formation and cytopathicity *in vivo*, and consequently, that the metalloproteinase pathway
374 is likely to be involved in the pathogenesis of COVID-19.
375
376 **Discussion**
377 Previous studies of the S proteins found in SARS-CoV-2, SARS-CoV, and MERS-CoV
378 have shown that the priming of the S2 domain, catalyzed by either TMPRSS2 on the
379 plasma membrane or cathepsin-B/L in endosomes, results in the fusion peptide protruding
380 to induce envelope fusion, thereby establishing viral entry through the plasma membrane
381 or endosomal membrane, respectively[14, 19, 20]. In this study, we have demonstrated
382 that SARS-CoV-2, unlike SARS-CoV or MERS-CoV, has a unique TMPRSS2-
383 independent cell surface entry pathway, which is sensitive to various metalloproteinase
384 inhibitors including ilomastat, CTS-1027, marimastat, and prinomastat, but resistant to
385 previously known inhibitors of SARS-CoV-2 entry, such as nafamostat[24, 46] and E-
386 64d[19]. As a representative of these broad-spectrum metalloproteinase inhibitors, we
387 chose marimastat to investigate the cell type-dependent distribution of the
388 metalloproteinase pathway by measuring pseudovirus infection. A significant proportion

bioRxiv preprint doi: https://doi.org/10.1101/2021.12.14.472513; this version posted December 15, 2021. The copyright holder for this preprint (which was not certified by peer review) is the author/funder, who has granted bioRxiv a license to display the preprint in perpetuity. It is made available under aCC-BY-NC-ND 4.0 International license.

of the entry pathway is metalloproteinase-dependent in A704 (kidney), HEC50B (endometrium), OVTOKO (ovary), and VeroE6 (kidney) cells. Only a small proportion was metalloproteinase-dependent in IGROV1 (ovary) cells, while the metalloproteinase pathway was not detected in OMUS-23 (colon), OVISE (ovary), Calu-3 (lung), and Caco-2 (colon) cells. These results indicate that the metalloproteinase pathway of SARS-CoV-2 is cell-type specific and independently coexists with other entry pathways, including the TMPRSS2-dependent surface pathway and the endosome pathway. The kidney[47, 48], ovary[49, 50], and endometrium[51] are known to express ACE2. Furthermore, SARS-CoV-2 can infect the kidney[48, 52] and induce acute kidney injury[53] in COVID-19 patients. Although SARS-CoV-2 infection of the ovary or endometrium has not previously been reported, the metalloproteinase-dependent infection pathway may contribute to the pathogenesis of COVID-19, especially multiple organ failure. The metalloproteinase pathway is thus a potential target for future COVID-19 therapies.

The S1/S2 boundary of SARS-CoV-2 contains the furin cleavage motif (Arg-X-X-Arg), while that of SARS-CoV contains only a single Arg. It has been reported that the motif greatly increases the efficiency of S1/S2 cleavage[15, 16], leading to enhanced viral transmission both *in vitro[15, 16, 23]* and *in vivo[54, 55]*. This may be partially due to the enhanced availability of S2 to TMPRSS2, due to the dissociation of S1[56, 57]. We

bioRxiv preprint doi: https://doi.org/10.1101/2021.12.14.472513; this version posted December 15, 2021. The copyright holder for this preprint (which was not certified by peer review) is the author/funder, who has granted bioRxiv a license to display the preprint in perpetuity. It is made available under aCC-BY-NC-ND 4.0 International license.

have shown that the furin cleavage motif is required for the metalloproteinase pathway, and we propose that the induction of metalloproteinase-induced S2 priming is another role of furin-mediated S1/S2 cleavage in enhanced viral transmission. Therefore, the metalloproteinase-dependent entry pathway, which is unique among highly pathogenic coronaviruses, is likely to be associated with the rapid spread of SARS-CoV-2. Interestingly, experiments using pseudoviruses bearing chimeric S proteins between SARS-CoV (without the metalloproteinase pathway) and SARS-CoV-2 (with the metalloproteinase pathway) revealed that both the S1/S2 boundary of SARS-CoV-2 and the S2 domain of SARS-CoV-2 S are essential for metalloproteinase-dependent entry. In contrast, the two domains of SARS-CoV-2 independently contributed to TMPRSS2-dependent S2 priming. This discrepancy may be partially due to the difference in the substrate recognition properties of the priming proteases in the two pathways. The S112 pseudovirus (a VSV pseudovirus bearing SARS-CoV S mutant, in which the S2 region was replaced with the corresponding domain of SARS-CoV-2) can use the TMPRSS2 pathway more efficiently than the SARS-CoV S pseudovirus, which suggests that TMPRSS2 may be partially accessible to the priming site in SARS-CoV-2 (C-terminal of Arg815) but not to that in SARS-CoV (C-terminal of Arg797) without S1 dissociation. In contrast, the putative priming protease in the metalloproteinase pathway, which may

bioRxiv preprint doi: https://doi.org/10.1101/2021.12.14.472513; this version posted December 15, 2021. The copyright holder for this preprint (which was not certified by peer review) is the author/funder, who has granted bioRxiv a license to display the preprint in perpetuity. It is made available under aCC-BY-NC-ND 4.0 International license.

not be a metalloproteinase but a protease activated by metalloproteinases, can access the priming site only when the site occurs within the contextual characteristics of SARS-CoV-2 S2, and S1/S2 is cleaved to allow S1 dissociation. Determination of the priming site in the metalloproteinase pathway and identification of the critical amino acid residues generating the structural characteristics of SARS-CoV-2 S2 that allow metalloproteinase-dependent priming are required to understand its molecular mechanisms for the two distinct surface entry pathways. From an evolutionary perspective, SARS-CoV-2 acquired the metalloproteinase pathway by introducing mutations into the S2 region, which may have contributed to the SARS-CoV-2 pandemic. The function of point mutations in the S2 domain have not yet been fully analyzed in comparison to those in the S1 domain, which cause escape from neutralizing antibodies[58]. However, various point mutations in the S2 domain may play important roles in increasing the efficiency of infection and disease progression and the generation of highly infectious variants.

Using selective metalloproteinase inhibitors and ADAM10 knockdowns generated using specific siRNAs, we have demonstrated that ADAM10 plays an important role in the metalloproteinase pathway. ADAM10 is ubiquitously expressed in various tissues[59] and cell lines[60], and functionally regulates cell differentiation and proliferation by cleaving ligands and receptors such as epidermal growth factor (EGF),

bioRxiv preprint doi: https://doi.org/10.1101/2021.12.14.472513; this version posted December 15, 2021. The copyright holder for this preprint (which was not certified by peer review) is the author/funder, who has granted bioRxiv a license to display the preprint in perpetuity. It is made available under aCC-BY-NC-ND 4.0 International license.

heparin-binding EGF-like growth factor (HB-EGF), and Notch[61]. ADAM10 is thus likely to contribute to SARS-CoV-2 infection in various organs. ADAM17, similar to ADAM10, is also known as a metalloproteinase that induces the cleavage of receptors and ligands, and both can cleave common substrates such as Notch and HB-EGF[61]. It has been reported that ACE2 shedding by ADAM17 promotes SARS-CoV-2 infection[42]. Although we observed that ADAM17 depletion resulted in the cellular accumulation of ACE2, which is indicative of reduced ACE2 shedding, total SARS-CoV-2 pseudovirus infection was unexpectedly augmented and the relative contribution of the metalloproteinase pathway was not affected. ADAM10 and ADAM17 thus both play crucial but distinct roles in SARS-CoV-2 infection. It has recently been reported that ADAM9 inhibition decreases SARS-CoV-2 infection *in vitro[62]*. Although the involvement of ADAM9 in viral entry is not clear, the results suggest that a group of metalloproteinases cooperate in the metalloproteinase pathway. This may indicate that the observed ADAM10 depletion-induced inhibition was a part of the maximum inhibition by various metalloproteinase inhibitors. A recent report also showed that MMP12 knockouts inhibited SARS-CoV-2 infection *in vitro[63]*. However, MMP408[30], an inhibitor of MMP12, did not prevent SARS-CoV-2 infection in various cell lines in this investigation, suggesting that metalloproteinases involved in the

bioRxiv preprint doi: https://doi.org/10.1101/2021.12.14.472513; this version posted December 15, 2021. The copyright holder for this preprint (which was not certified by peer review) is the author/funder, who has granted bioRxiv a license to display the preprint in perpetuity. It is made available under aCC-BY-NC-ND 4.0 International license.

metalloproteinase pathway may differ in a cell type-dependent manner. Further studies are required to identify the functional metalloproteinases that are involved in the metalloproteinase pathway.

Various compounds are reported to inhibit SARS-CoV-2 infection by inhibiting envelope fusion *in vitro*. However, camostat[64], an inhibitor of the TMPRSS2-dependent surface entry, and hydroxychloroquine[65, 66], an inhibitor of the endosomal pathway, have failed to show sufficient therapeutic efficacy in clinical trials. Our entry pathway analysis revealed that the metalloproteinase surface pathway coexists with the TMPRSS2 pathway and/or the endosome pathway in various cell types. Furthermore, in HEC50B and HEC50B-TMPRSS2 cells, cell death could not be inhibited unless all entry pathways in each cell were inhibited using inhibitor co-treatments for each pathway. Therefore, future clinical trials on virus entry in which the TMPRSS2, metalloproteinase, and endosome pathways are all efficiently blocked, need to be conducted. We propose that to address this challenge both marimastat and prinomastat should be utilized in clinical trials. The mean maximum plasma concentration ($C_{max}$) at a reasonably well-tolerated dose was 590 nM for marimastat[27] and 680 nM for prinomastat[28]. Furthermore, we demonstrated that these two drugs significantly inhibited SARS-CoV-2 infection at concentrations lower than their $C_{max}$ values. These metalloprotease inhibitors,

bioRxiv preprint doi: https://doi.org/10.1101/2021.12.14.472513; this version posted December 15, 2021. The copyright holder for this preprint (which was not certified by peer review) is the author/funder, who has granted bioRxiv a license to display the preprint in perpetuity. It is made available under aCC-BY-NC-ND 4.0 International license.

in combination with other protease inhibitors targeting the TMPRSS2 and endosome pathways, may effectively inhibit SARS-CoV-2 infection in various tissues and cure COVID-19. Recently, there has been concern about the spread of SARS-CoV-2 variants, such as the delta strain, as they reduce the effectiveness of the neutralizing antibodies produced by vaccination[7, 9, 10]. Since sensitivities against marimastat, nafamostat, and E-64d have been conserved in the various variants investigated so far, the strategies to use protease inhibitors for COVID-19 treatment are likely to be significantly effective against these variants. The results of this study may contribute to the development of COVID-19 treatments targeting viral entry pathways.

## Materials and Methods

### Cell lines, viruses, and reagents

VeroE6 (CRL-1586), 293T (CRL-3216), A704 (HTB-45) and Calu-3 (HTB-55) cells were obtained from the American Type Culture Collection (Rockville, MD, USA). OVTOKO (JCRB1048), OVISE (JCRB1043), HEC50B (JCRB1145), VeroE6-TMPRSS2 (JCRB1819)[67], and OUMS-23 (JCRB1022) cells were obtained from the Japanese Collection of Research Bioresources Cell Bank (Osaka, Japan). IGROV1 cells (SCC203) were purchased from Merck (Darmstadt, Germany) and Caco-2 cells

bioRxiv preprint doi: https://doi.org/10.1101/2021.12.14.472513; this version posted December 15, 2021. The copyright holder for this preprint (which was not certified by peer review) is the author/funder, who has granted bioRxiv a license to display the preprint in perpetuity. It is made available under aCC-BY-NC-ND 4.0 International license.

(RCB0988) were obtained from the RIKEN BioResource Research Center (Tsukuba, Japan). A704, Calu-3, VeroE6, HEC50B, and Caco-2 cells were maintained in Eagle's minimum essential medium (EMEM; 055-08975, FUJIFILM Wako Pure Chemical, Osaka, Japan) containing 15% fetal bovine serum (FBS). OUMS-23, IGROV1, and 293T cells were maintained in Dulbecco's modified Eagle's medium (DMEM; 041-30081, FUJIFILM Wako Pure Chemical) containing 10% FBS. VeroE6-TMPRSS2 (JCRB1819) cells were cultured in DMEM containing 10% FBS and 1 mg/mL G418. OVISE and OVTOKO cells were maintained in Roswell Park Memorial Institute (RPMI)-1640 medium (189-02025, FUJIFILM Wako Pure Chemical) containing 10% FBS. A pair of previously described 293FT-based reporter cell lines that stably express individual split reporters (DSP1-7 and DSP8-11 proteins)[68] were maintained in DMEM containing 10% FBS and 1 μg/mL puromycin. To establish stable cell lines expressing the S protein of SARS-CoV, SARS-CoV-2, or MERS-CoV, recombinant pseudotype lentiviruses were produced in 293T cells with psPAX2 packaging plasmid, vesicular stomatitis virus (VSV)-G-expressing plasmid and lentiviral transfer plasmid expressing S protein. To establish stable cell lines expressing ACE2 or CD26 with TMPRSS2, recombinant pseudotype lentiviruses expressing one of the proteins were produced using 293T cells with psPAX2 packaging plasmid and VSV-G-expressing plasmid. The 293FT-derived

bioRxiv preprint doi: https://doi.org/10.1101/2021.12.14.472513; this version posted December 15, 2021. The copyright holder for this preprint (which was not certified by peer review) is the author/funder, who has granted bioRxiv a license to display the preprint in perpetuity. It is made available under aCC-BY-NC-ND 4.0 International license.

reporter cells infected with the pseudotype viruses were selected with 1 μg/mL puromycin, 10 μg/mL blasticidin, and 300 μg/mL hygromycin for at least 1 week. These bulk-selected cells were used for fusion assays. To establish HEC50B cells expressing TMPRSS2 (HEC50B-TMPRSS2), recombinant pseudotype lentivirus expressing TMPRSS2 was produced using 293T cells with psPAX2 packaging plasmid and VSV-G-expressing plasmid. HEC50B cells infected with pseudotype viruses were selected with 300 μg/mL hygromycin for at least 1 week. The SARS-CoV-2 isolate (UT-NCGM02/Human/2020/Tokyo)[69] was propagated in VeroE6-TMPRSS2 (JCRB1819) cells in DMEM containing 5% FBS. Titers were determined with plaque assays using VeroE6/TMPRSS2 (JCRB1819) cells. Negative control No.1 siRNA (4390843), negative control No.2 siRNA (4390846), and three distanced ADAM10-specific siRNAs were purchased from Thermo Fisher Scientific (MA, USA) The siRNA sequences used were 5′-UCA CCU UGU UCU ACC AUU CCA (S1004, ADAM10#1); 5′-UAA CCU CUA AAA UCG UUG CAA (S1005, ADAM10#2); and 5′-UAC GGA UUC CGG AGA AGU CTG (S1006, ADAM10#3) for the ADAM10 knockdown. Cell viability was analyzed using the CellTiter-Glo luminescent cell viability assay (G7570, Promega, WI, USA) according to the manufacturer's protocol.

bioRxiv preprint doi: https://doi.org/10.1101/2021.12.14.472513; this version posted December 15, 2021. The copyright holder for this preprint (which was not certified by peer review) is the author/funder, who has granted bioRxiv a license to display the preprint in perpetuity. It is made available under aCC-BY-NC-ND 4.0 International license.

**Protease inhibitors and compound libraries**

Nafamostat mesylate (N0959, Tokyo Chemical Industry, Tokyo, Japan), pepstatin A (4397, Peptide institute, Osaka, Japan), bestatin (027-14101, FUJIFILM Wako Pure Chemical), leupeptin (4041, Peptide institute), E-64d (4321-v, Peptide institute), furin inhibitor II (344931, Merck), ilomastat (HY-15768, MedChemExpress, NJ, USA), CTS-1027 (HY-10398, MedChemExpress), marimastat (HY-12169, MedChemExpress), prinomastat hydrochloride (PZ0198, Sigma-Aldrich, MO, USA), UK370106 (2900, Tocris, MN, USA), GW280264X (31388, Cayman, MI, USA), GI254023X (SML0789, Sigma-Aldrich), TAPI-2 (14695, Cayman), MLN-4760 (530616, Merck), BK-1361 (PC-60981, ProbeChem, Shanghai, China), MMP408 (444291, Millipore, MA, USA), MMP2/9 inhibitor I (ab145190, Abcam, Cambridge, UK), and MMP9 inhibitor I (444278, Millipore) were dissolved in dimethyl sulfoxide (DMSO) at a concentration of 10 mM. Validated Compound Library (1,630 clinically approved compounds and 1,885 pharmacologically active compounds) obtained from the Drug Discovery Initiative (The University of Tokyo) was used for compound screening.

**Expression vector construction**

bioRxiv preprint doi: https://doi.org/10.1101/2021.12.14.472513; this version posted December 15, 2021. The copyright holder for this preprint (which was not certified by peer review) is the author/funder, who has granted bioRxiv a license to display the preprint in perpetuity. It is made available under aCC-BY-NC-ND 4.0 International license.

To construct expression vectors for ACE2, CD26, and TMPRSS2, genes were cloned into a lentiviral transfer plasmid (CD500B-1, SBI, Palo Alto, CA, USA). Synthetic DNA corresponding to the codon-optimized S gene of SARS-CoV-2 (Wuhan-Hu-1, RefSeq: NC_045512.2), SARS-CoV-2 variants (B.1.1.7, GISAID: EPI_ISL_601443, B.1.351, GenBank: MZ747297.1, B.1.617.1, GISAID: EPI_ISL_1704611, B.1.617.2, GISAID: EPI_ISL_3189054), SARS-CoV (Tor2, RefSeq: NC_004718.3), bat SARS-like coronavirus WIV1 (GenBank: KF367457.1), human coronavirus NL63 (RefSeq: NC_005831.2), and the chimeric S gene (S1, S1/S2 boundary, and S2 domains were derived from either SARS-CoV Tor2 or SARS-Cov-2 Wuhan-Hu-1), and the DNA sequence corresponding to the Flag-tag 5′-GGA GGC GAT TAC AAG GAT GAC GAT GAC AAG TAA-3’ (underline, Flag-tag) at the 3′ end were all generated by Integrated DNA Technologies (IA, USA). Previously described synthetic DNA corresponding to the codon-optimized S gene of a MERS-CoV (EMC 2012, RefSeq: NC_019843.3)[25] with a DNA sequence corresponding to the Flag-tag 5′-GGA GGC GAT TAC AAG GAT GAC GAT GAC AAG TAA-3’ at the 3′ end was used in this study. To construct expression vectors for the S protein, the coding regions were cloned into a lentiviral transfer plasmid (CD500B-1, SBI).

bioRxiv preprint doi: https://doi.org/10.1101/2021.12.14.472513; this version posted December 15, 2021. The copyright holder for this preprint (which was not certified by peer review) is the author/funder, who has granted bioRxiv a license to display the preprint in perpetuity. It is made available under aCC-BY-NC-ND 4.0 International license.

568 **DSP assay to monitor membrane fusion**

569 DSP1-7 has the structure $RL_{1–155}$-Ser-Gly-Gly-Gly-Gly-$GFP_{1–156}$, while DSP8-11 has the
570 structure Met-$GFP_{157–231}$-Gly-Gly-Gly-Gly-Ser- $RL_{156–311}$. RL and GFP become active
571 only when DSP1-7 associates with DSP-8-11 (S1c Fig). For the DSP assay using 293FT
572 cells, DSP8-11 expressing effector cells expressing S protein and DSP1-7 expressing
573 target cells expressing CD26 or ACE2 alone or together with TMPRSS2 were seeded in
574 10 cm cell culture plates ($4 \times 10^6$ cells/10 mL) one day prior to the assay (S1a,b Fig).
575 Cells were treated with 6 μM EnduRen (Promega), a substrate for Renilla luciferase (RL),
576 for 2 h to activate EnduRen. For compound library screening, 0.25 μL of each compound
577 dissolved in DMSO were added to the 384-well plates (Greiner Bioscience,
578 Frickenhausen, Germany). To test the effects of the selected inhibitors, 1 μL of each
579 inhibitor dissolved in DMSO was added to the 384-well plates (Greiner Bioscience). Next,
580 50 μL of each single cell suspension (effector and target cells) was added to the 384-well
581 plates using a Multidrop dispenser (Thermo Fisher Scientific, MA, USA). After
582 incubation at 37 °C in 5% $CO_2$ for 4 h, the RL activity was measured using a Centro
583 xS960 luminometer (Berthold, Bad Wildbad, Germany).

584

585 **Western blotting**

bioRxiv preprint doi: https://doi.org/10.1101/2021.12.14.472513; this version posted December 15, 2021. The copyright holder for this preprint (which was not certified by peer review) is the author/funder, who has granted bioRxiv a license to display the preprint in perpetuity. It is made available under aCC-BY-NC-ND 4.0 International license.

586 Western blot analysis was performed as described previously[70]. The primary antibodies
587 used were rabbit anti-ACE2 (1:1000, ab15348, Abcam), rabbit anti-TACE (1:1000,
588 3976S, Cell Signaling Technology, MA, USA), rabbit anti-ADAM10 (1:1000, 14194S,
589 Cell Signaling Technology), rabbit anti-Flag-tag (1:1000, PM020, MBL, MA, USA),
590 mouse anti-tubulin (1:1000, CP06, Millipore), and mouse anti-VSVM (1:1000, 23H12,
591 Absolute antibody). The Secondly antibodies used were HRP-linked donkey anti-rabbit
592 IgG antibody (NA934; GE Healthcare, Piscataway, NJ, USA) and HRP-linked donkey
593 anti-mouse IgG antibody (NA931V; GE Healthcare). Cell supernatants containing the
594 pseudotype viral particles were centrifuged at 109,000 g or 35 min at 4 ℃ using a
595 TLA100.3 rotor with an Optima TLX ultracentrifuge (Beckman Coulter, CA, USA), and
596 the pellet was then lysed for western blotting analysis.
597
598 **Preparation of pseudotype VSV viral particles and infection experiments**
599 To prepare pseudotype VSV viral particles 293T cells were transfected with an expression
600 plasmid for S, VSV G, or a control expression plasmid using calcium phosphate
601 precipitation. At 16 h post-transfection, the cells were inoculated with a replication-
602 deficient VSV, Δ VSV-Luci, which lacks the VSV G gene and encodes firefly luciferase,
603 at a multiplicity of infection (MOI) of 1, as was described previously[71]. After

bioRxiv preprint doi: https://doi.org/10.1101/2021.12.14.472513; this version posted December 15, 2021. The copyright holder for this preprint (which was not certified by peer review) is the author/funder, who has granted bioRxiv a license to display the preprint in perpetuity. It is made available under aCC-BY-NC-ND 4.0 International license.

604 incubation at 37 °C in 5% $CO_2$ for 2 h, the cells were washed with DMEM and further
605 incubated at 37 °C in 5% $CO_2$ for 16 h before the supernatants containing the pseudotype
606 viral particles were harvested. Cellular debris was removed from the supernatants using
607 a syringe filter with a 0.45 μm size pore (Millipore). For the infection assay, target cells
608 were seeded in 96-well plates ($2 \times 10^4$ cells/well) and incubated overnight at 37 °C with
609 5% $CO_2$. The cells were pre-treated with inhibitors for 1 h before infection. Pseudotype
610 viral particles were added to the cells in the presence of the inhibitors. Luciferase activity
611 was measured 16 h post-infection using the Bright-Glo Luciferase Assay System or ONE-
612 Glo Luciferase Assay System (Promega) and Centro xS960 luminometer (Berthold).
613
614 **Transfection**
615 siRNA transfection was performed using Lipofectamine RNAiMAX (Thermo Fisher
616 Scientific) according to the manufacturer's protocol. Cells were seeded in 6-well plates
617 ($1.6 \times 10^6$ cells/well) with siRNA and Lipofectamine RNAiMAX. Then 24 h after
618 transfection, the cells were seeded in 96-well plates ($2 \times 10^4$ cells/well), and 48 h after
619 transfection the cells were used for the infection experiments.
620
621 **Quantification of intracellular SARS-CoV-2 RNA**

bioRxiv preprint doi: https://doi.org/10.1101/2021.12.14.472513; this version posted December 15, 2021. The copyright holder for this preprint (which was not certified by peer review) is the author/funder, who has granted bioRxiv a license to display the preprint in perpetuity. It is made available under aCC-BY-NC-ND 4.0 International license.

622 Cells were seeded at 5 × $10^4$ cells per well in a 96-well cell culture plate. After an
623 overnight incubation at 37 °C in 5% $CO_2$, cells were treated with protease inhibitors for
624 1 h and added with SARS-CoV-2 at a multiplicity of infection (MOI) of 0.01 for HEC50B
625 and HEC50B-TMPRSS2 cells, and MOI of 0.1 for VeroE6, Calu-3, and A704 cells. After
626 24 h of incubation at 37 °C in 5% $CO_2$, the cells were washed three times with PBS. Cell
627 lysis and cDNA synthesis were performed using SuperPrep II Cell Lysis & RT Kit for
628 qPCR (SCQ-401, TOYOBO, Osaka, Japan) following the manufacturer's instructions.
629 SARS-CoV-2 RNA was detected using a primer set targeting the SARS-CoV-2 N gene.
630 Quantitative real-time RT-PCR was performed using THUNDERBIRD SYBR qPCR
631 Mix (TOYOBO) at 95 °C for 3 min, followed by 50 cycles of 95 °C for 10 s and 60 °C
632 for 1 min. Fluorescence was detected during the thermal cycling process, and
633 quantification studies were performed using the CFX ConnectTM Real-Time PCR
634 detection system (Bio-Rad, CA, USA). The level of ribosomal protein L13a (*Rpl13a*)
635 mRNA expression in each sample was used to standardize the data. The primer sequences
636 used were 5′-AAA TTT TGG GGA CCA GGA AC-3' (forward primer) and 5′-TGG CAG
637 CTG TGT AGG TCA AC-3' (reverse primer) for the SARS-CoV-2 N gene; 5′-TGT TTG
638 ACG GCA TCC CAC-3' (forward primer) and 5′-CTG TCA CTG CCT GGT ACT TC-
639 3' (reverse primer) for human *Rpl13a* gene; and 5′-CTC AAG GTT GTG CGT CTG AA-

bioRxiv preprint doi: https://doi.org/10.1101/2021.12.14.472513; this version posted December 15, 2021. The copyright holder for this preprint (which was not certified by peer review) is the author/funder, who has granted bioRxiv a license to display the preprint in perpetuity. It is made available under aCC-BY-NC-ND 4.0 International license.

3' (forward primer) and 5′-CTG TCA CTG CCT GGT ACT TCC A-3' (reverse primer) for the African green monkey *Rpl13a* gene.

**Immunofluorescence Staining**

HEC50B and HEC50B-TMPRSS2 cells were seeded at $1.5 \times 10^5$ cells per well in a 24-well cell culture plate. After an overnight incubation at 37 ℃ in 5% $CO_2$, cells were treated with protease inhibitors for 1 h and then with SARS-CoV-2 at an MOI of 1. After 24 h of incubation at 37 ℃ in 5% $CO_2$, cells were fixed with 4% paraformaldehyde in PBS(-) for 10 min at RT and then permeabilized with 0.1% Triton X-100 in PBS(-) for 10 min at RT. Cells were then incubated with anti-SARS-CoV-2 nucleocapsid (1:1000, GTX135357, GeneTex, CA, USA) primary antibody for 16 h at 4 ℃ and detected with anti-rabbit-Alexa488 (1:200, A11008, Invitrogen, CA, USA) secondary antibodies for 40 min at RT. Cell nuclei were stained with 1 μg/mL Hoechst 33342 (#080-09981, FUJIFILM Wako Pure Chemical). Fluorescent signals were detected using a BZ-X810 fluorescent microscope (Keyence, Osaka, Japan).

**Cytopathicity assay**

bioRxiv preprint doi: https://doi.org/10.1101/2021.12.14.472513; this version posted December 15, 2021. The copyright holder for this preprint (which was not certified by peer review) is the author/funder, who has granted bioRxiv a license to display the preprint in perpetuity. It is made available under aCC-BY-NC-ND 4.0 International license.

657 HEC50B and HEC50B-TMPRSS2 cells were seeded at $1.5 \times 10^5$ cells per well in a 24-
658 well cell culture plate. After an overnight incubation at 37 °C in 5% $CO_2$, cells were
659 treated with protease inhibitors for 1 h and then with SARS-CoV-2 at an MOI of 1. To
660 maintain the drug concentration, half of the culture supernatant was replaced daily with
661 fresh medium that contained drugs. After incubation at 37 °C in 5% $CO_2$ for 3 d, the cells
662 were fixed with 4% paraformaldehyde in PBS for 10 min at 25 °C and stained with 0.2%
663 crystal violet solution for 5 min. After washing four times with water, the wells were air-
664 dried at 25 °C. Ethanol was added to each well to dissolve crystal violet. The absorbance
665 was measured at 595 nm using an iMarkTM Microplate Reader (Bio-Rad).
666
667 **Statistical analysis**
668 Statistical analyses were performed in Microsoft Excel 2016 (Microsoft, Redmond, WA,
669 USA) and GraphPad Prism 8 (GraphPad Software, San Diego, CA). Statistically
670 significant differences between the mean values were determined using a two-tailed
671 Student's t-test. Dunnett's test and Tukey's test were used for multiple comparisons. All
672 data represent three independent experiments, and values represent the mean ± standard
673 deviation (s.d.), with a $p < 0.05$, considered statistically significant.
674

bioRxiv preprint doi: https://doi.org/10.1101/2021.12.14.472513; this version posted December 15, 2021. The copyright holder for this preprint (which was not certified by peer review) is the author/funder, who has granted bioRxiv a license to display the preprint in perpetuity. It is made available under aCC-BY-NC-ND 4.0 International license.

## Acknowledgements

We thank Yoshihiro Kawaoka for providing the SARS-CoV-2 isolate (UT-NCGM/Human/2020/Tokyo), Robert Whittier for critical reading of our manuscript and Kinuyo Miyazaki for her secretarial assistance.

## Author contributions

M.Y., J.G., and J.I. designed the study; M.Y., J.G., A.K., K.T., and Y.H. performed the experiments; M.Y., J.G., N.K., M.S., K.S., T.A., Y.K., and J.I. analyzed and interpreted the data; and M.Y. and J.I. wrote the manuscript.

## References

1. Zhou P, Yang XL, Wang XG, Hu B, Zhang L, Zhang W, et al. A pneumonia outbreak associated with a new coronavirus of probable bat origin. Nature. 2020;579(7798):270-3. Epub 2020/02/03. doi: 10.1038/s41586-020-2012-7. PubMed PMID: 32015507; PubMed Central PMCID: PMCPMC7095418.

2. Zhong NS, Zheng BJ, Li YM, Poon, Xie ZH, Chan KH, et al. Epidemiology and cause of severe acute respiratory syndrome (SARS) in Guangdong, People's Republic of China, in February, 2003. Lancet. 2003;362(9393):1353-8. doi: 10.1016/s0140-6736(03)14630-2.

bioRxiv preprint doi: https://doi.org/10.1101/2021.12.14.472513; this version posted December 15, 2021. The copyright holder for this preprint (which was not certified by peer review) is the author/funder, who has granted bioRxiv a license to display the preprint in perpetuity. It is made available under aCC-BY-NC-ND 4.0 International license.

693 PubMed PMID: 14585636; PubMed Central PMCID: PMCPMC7112415.

694 3. Drosten C, Günther S, Preiser W, van der Werf S, Brodt HR, Becker S, et al.

695 Identification of a novel coronavirus in patients with severe acute respiratory syndrome. N

696 Engl J Med. 2003;348(20):1967-76. Epub 20030410. doi: 10.1056/NEJMoa030747. PubMed

697 PMID: 12690091.

698 4. Zaki AM, van Boheemen S, Bestebroer TM, Osterhaus AD, Fouchier RA. Isolation

699 of a novel coronavirus from a man with pneumonia in Saudi Arabia. N Engl J Med.

700 2012;367(19):1814-20. doi: 10.1056/NEJMoa1211721. PubMed PMID: 23075143.

701 5. Harrison AG, Lin T, Wang P. Mechanisms of SARS-CoV-2 Transmission and

702 Pathogenesis. Trends Immunol. 2020;41(12):1100-15. Epub 20201014. doi:

703 10.1016/j.it.2020.10.004. PubMed PMID: 33132005; PubMed Central PMCID:

704 PMCPMC7556779.

705 6. Hu B, Guo H, Zhou P, Shi ZL. Characteristics of SARS-CoV-2 and COVID-19. Nat

706 Rev Microbiol. 2021;19(3):141-54. Epub 20201006. doi: 10.1038/s41579-020-00459-7. PubMed

707 PMID: 33024307; PubMed Central PMCID: PMCPMC7537588.

708 7. Tregoning JS, Flight KE, Higham SL, Wang Z, Pierce BF. Progress of the COVID-

709 19 vaccine effort: viruses, vaccines and variants versus efficacy, effectiveness and escape. Nat

710 Rev Immunol. 2021;21(10):626-36. Epub 20210809. doi: 10.1038/s41577-021-00592-1.

bioRxiv preprint doi: https://doi.org/10.1101/2021.12.14.472513; this version posted December 15, 2021. The copyright holder for this preprint (which was not certified by peer review) is the author/funder, who has granted bioRxiv a license to display the preprint in perpetuity. It is made available under aCC-BY-NC-ND 4.0 International license.

711 PubMed PMID: 34373623; PubMed Central PMCID: PMCPMC8351583.

712 8. Pritchard E, Matthews PC, Stoesser N, Eyre DW, Gethings O, Vihta KD, et al.

713 Impact of vaccination on new SARS-CoV-2 infections in the United Kingdom. Nat Med.

714 2021;27(8):1370-8. Epub 20210609. doi: 10.1038/s41591-021-01410-w. PubMed PMID:

715 34108716; PubMed Central PMCID: PMCPMC8363500.

716 9. Planas D, Veyer D, Baidaliuk A, Staropoli I, Guivel-Benhassine F, Rajah MM, et al.

717 Reduced sensitivity of SARS-CoV-2 variant Delta to antibody neutralization. Nature.

718 2021;596(7871):276-80. Epub 20210708. doi: 10.1038/s41586-021-03777-9. PubMed PMID:

719 34237773.

720 10. Tao K, Tzou PL, Nouhin J, Gupta RK, de Oliveira T, Kosakovsky Pond SL, et al. The

721 biological and clinical significance of emerging SARS-CoV-2 variants. Nat Rev Genet. 2021.

722 Epub 20210917. doi: 10.1038/s41576-021-00408-x. PubMed PMID: 34535792; PubMed

723 Central PMCID: PMCPMC8447121.

724 11. Uriu K, Kimura I, Shirakawa K, Takaori-Kondo A, Nakada TA, Kaneda A, et al.

725 Neutralization of the SARS-CoV-2 Mu Variant by Convalescent and Vaccine Serum. N Engl

726 J Med. 2021. Epub 20211103. doi: 10.1056/NEJMc2114706. PubMed PMID: 34731554.

727 12. Mei M, Tan X. Current Strategies of Antiviral Drug Discovery for COVID-19. Front

728 Mol Biosci. 2021;8:671263. Epub 20210513. doi: 10.3389/fmolb.2021.671263. PubMed PMID:

bioRxiv preprint doi: https://doi.org/10.1101/2021.12.14.472513; this version posted December 15, 2021. The copyright holder for this preprint (which was not certified by peer review) is the author/funder, who has granted bioRxiv a license to display the preprint in perpetuity. It is made available under aCC-BY-NC-ND 4.0 International license.

729 34055887; PubMed Central PMCID: PMCPMC8155633.

730 13. Rando HM, Wellhausen N, Ghosh S, Lee AJ, Dattoli AA, Hu F, et al. Identification

731 and Development of Therapeutics for COVID-19. mSystems. 2021:e0023321. Epub 20211102.

732 doi: 10.1128/mSystems.00233-21. PubMed PMID: 34726496; PubMed Central PMCID:

733 PMCPMC8562484.

734 14. Jackson CB, Farzan M, Chen B, Choe H. Mechanisms of SARS-CoV-2 entry into

735 cells. Nat Rev Mol Cell Biol. 2021. Epub 20211005. doi: 10.1038/s41580-021-00418-x. PubMed

736 PMID: 34611326; PubMed Central PMCID: PMCPMC8491763.

737 15. Hoffmann M, Kleine-Weber H, Pöhlmann S. A Multibasic Cleavage Site in the Spike

738 Protein of SARS-CoV-2 Is Essential for Infection of Human Lung Cells. Mol Cell.

739 2020;78(4):779-84.e5. Epub 20200501. doi: 10.1016/j.molcel.2020.04.022. PubMed PMID:

740 32362314; PubMed Central PMCID: PMCPMC7194065.

741 16. Shang J, Wan Y, Luo C, Ye G, Geng Q, Auerbach A, et al. Cell entry mechanisms of

742 SARS-CoV-2. Proc Natl Acad Sci U S A. 2020;117(21):11727-34. Epub 2020/05/06. doi:

743 10.1073/pnas.2003138117. PubMed PMID: 32376634.

744 17. Yan R, Zhang Y, Li Y, Xia L, Guo Y, Zhou Q. Structural basis for the recognition of

745 SARS-CoV-2 by full-length human ACE2. Science. 2020;367(6485):1444-8. Epub 20200304.

746 doi: 10.1126/science.abb2762. PubMed PMID: 32132184; PubMed Central PMCID:

bioRxiv preprint doi: https://doi.org/10.1101/2021.12.14.472513; this version posted December 15, 2021. The copyright holder for this preprint (which was not certified by peer review) is the author/funder, who has granted bioRxiv a license to display the preprint in perpetuity. It is made available under aCC-BY-NC-ND 4.0 International license.

PMCPMC7164635.

18. Lan J, Ge J, Yu J, Shan S, Zhou H, Fan S, et al. Structure of the SARS-CoV-2 spike receptor-binding domain bound to the ACE2 receptor. Nature. 2020;581(7807):215-20. Epub 20200330. doi: 10.1038/s41586-020-2180-5. PubMed PMID: 32225176.

19. Hoffmann M, Kleine-Weber H, Schroeder S, Krüger N, Herrler T, Erichsen S, et al. SARS-CoV-2 Cell Entry Depends on ACE2 and TMPRSS2 and Is Blocked by a Clinically Proven Protease Inhibitor. Cell. 2020;181(2):271-80.e8. Epub 2020/03/05. doi: 10.1016/j.cell.2020.02.052. PubMed PMID: 32142651; PubMed Central PMCID: PMCPMC7102627.

20. Zhao MM, Yang WL, Yang FY, Zhang L, Huang WJ, Hou W, et al. Cathepsin L plays a key role in SARS-CoV-2 infection in humans and humanized mice and is a promising target for new drug development. Signal Transduct Target Ther. 2021;6(1):134. Epub 20210327. doi: 10.1038/s41392-021-00558-8. PubMed PMID: 33774649; PubMed Central PMCID: PMCPMC7997800.

21. Murgolo N, Therien AG, Howell B, Klein D, Koeplinger K, Lieberman LA, et al. SARS-CoV-2 tropism, entry, replication, and propagation: Considerations for drug discovery and development. PLoS Pathog. 2021;17(2):e1009225. Epub 2021/02/17. doi: 10.1371/journal.ppat.1009225. PubMed PMID: 33596266; PubMed Central PMCID:

bioRxiv preprint doi: https://doi.org/10.1101/2021.12.14.472513; this version posted December 15, 2021. The copyright holder for this preprint (which was not certified by peer review) is the author/funder, who has granted bioRxiv a license to display the preprint in perpetuity. It is made available under aCC-BY-NC-ND 4.0 International license.

765 PMCPMC7888651.

766 22. Koch J, Uckeley ZM, Doldan P, Stanifer M, Boulant S, Lozach PY. TMPRSS2

767 expression dictates the entry route used by SARS-CoV-2 to infect host cells. EMBO J.

768 2021;40(16):e107821. Epub 20210713. doi: 10.15252/embj.2021107821. PubMed PMID:

769 34159616; PubMed Central PMCID: PMCPMC8365257.

770 23. Bestle D, Heindl MR, Limburg H, Van Lam van T, Pilgram O, Moulton H, et al.

771 TMPRSS2 and furin are both essential for proteolytic activation of SARS-CoV-2 in human

772 airway cells. Life Sci Alliance. 2020;3(9). Epub 20200723. doi: 10.26508/lsa.202000786.

773 PubMed PMID: 32703818; PubMed Central PMCID: PMCPMC7383062.

774 24. Yamamoto M, Kiso M, Sakai-Tagawa Y, Iwatsuki-Horimoto K, Imai M, Takeda M,

775 et al. The Anticoagulant Nafamostat Potently Inhibits SARS-CoV-2 S Protein-Mediated

776 Fusion in a Cell Fusion Assay System and Viral Infection In Vitro in a Cell-Type-Dependent

777 Manner. Viruses. 2020;12(6). Epub 2020/06/10. doi: 10.3390/v12060629. PubMed PMID:

778 32532094.

779 25. Yamamoto M, Matsuyama S, Li X, Takeda M, Kawaguchi Y, Inoue JI, et al.

780 Identification of Nafamostat as a Potent Inhibitor of Middle East Respiratory Syndrome

781 Coronavirus S Protein-Mediated Membrane Fusion Using the Split-Protein-Based Cell-Cell

782 Fusion Assay. Antimicrob Agents Chemother. 2016;60(11):6532-9. Epub 2016/08/24. doi:

bioRxiv preprint doi: https://doi.org/10.1101/2021.12.14.472513; this version posted December 15, 2021. The copyright holder for this preprint (which was not certified by peer review) is the author/funder, who has granted bioRxiv a license to display the preprint in perpetuity. It is made available under aCC-BY-NC-ND 4.0 International license.

783 10.1128/aac.01043-16. PubMed PMID: 27550352; PubMed Central PMCID:
784 PMCPMC5075056.
785 26. Ishikawa H, Meng F, Kondo N, Iwamoto A, Matsuda Z. Generation of a dual-
786 functional split-reporter protein for monitoring membrane fusion using self-associating split
787 GFP. Protein Eng Des Sel. 2012;25(12):813-20. doi: 10.1093/protein/gzs051. PubMed PMID:
788 22942393.
789 27. Wojtowicz-Praga S, Torri J, Johnson M, Steen V, Marshall J, Ness E, et al. Phase I
790 trial of Marimastat, a novel matrix metalloproteinase inhibitor, administered orally to
791 patients with advanced lung cancer. J Clin Oncol. 1998;16(6):2150-6. doi:
792 10.1200/JCO.1998.16.6.2150. PubMed PMID: 9626215.
793 28. Hande KR, Collier M, Paradiso L, Stuart-Smith J, Dixon M, Clendeninn N, et al.
794 Phase I and pharmacokinetic study of prinomastat, a matrix metalloprotease inhibitor. Clin
795 Cancer Res. 2004;10(3):909-15. doi: 10.1158/1078-0432.ccr-0981-3. PubMed PMID: 14871966.
796 29. Standard of Care (SOC) With or Without CTS-1027 in Hepatitis C (HCV) Null-
797 Responders https://clinicaltrials.gov/ct2/show/results/NCT01273064.
798 30. Vandenbroucke RE, Dejonckheere E, Libert C. A therapeutic role for matrix
799 metalloproteinase inhibitors in lung diseases? Eur Respir J. 2011;38(5):1200-14. Epub
800 20110609. doi: 10.1183/09031936.00027411. PubMed PMID: 21659416.

bioRxiv preprint doi: https://doi.org/10.1101/2021.12.14.472513; this version posted December 15, 2021. The copyright holder for this preprint (which was not certified by peer review) is the author/funder, who has granted bioRxiv a license to display the preprint in perpetuity. It is made available under aCC-BY-NC-ND 4.0 International license.

801 31. Jacobsen JA, Major Jourden JL, Miller MT, Cohen SM. To bind zinc or not to bind
802 zinc: an examination of innovative approaches to improved metalloproteinase inhibition.
803 Biochim Biophys Acta. 2010;1803(1):72-94. Epub 20090825. doi:
804 10.1016/j.bbamcr.2009.08.006. PubMed PMID: 19712708.
805 32. Madoux F, Dreymuller D, Pettiloud JP, Santos R, Becker-Pauly C, Ludwig A, et al.
806 Discovery of an enzyme and substrate selective inhibitor of ADAM10 using an exosite-
807 binding glycosylated substrate. Sci Rep. 2016;6(1):11. Epub 20161205. doi: 10.1038/s41598-
808 016-0013-4. PubMed PMID: 28442704; PubMed Central PMCID: PMCPMC5431342.
809 33. Liechti FD, Bächtold F, Grandgirard D, Leppert D, Leib SL. The matrix
810 metalloproteinase inhibitor RS-130830 attenuates brain injury in experimental
811 pneumococcal meningitis. J Neuroinflammation. 2015;12:43. Epub 20150304. doi:
812 10.1186/s12974-015-0257-0. PubMed PMID: 25890041; PubMed Central PMCID:
813 PMCPMC4352253.
814 34. Hundhausen C, Misztela D, Berkhout TA, Broadway N, Saftig P, Reiss K, et al. The
815 disintegrin-like metalloproteinase ADAM10 is involved in constitutive cleavage of CX3CL1
816 (fractalkine) and regulates CX3CL1-mediated cell-cell adhesion. Blood. 2003;102(4):1186-95.
817 Epub 20030424. doi: 10.1182/blood-2002-12-3775. PubMed PMID: 12714508.
818 35. Ludwig A, Hundhausen C, Lambert MH, Broadway N, Andrews RC, Bickett DM, et

bioRxiv preprint doi: https://doi.org/10.1101/2021.12.14.472513; this version posted December 15, 2021. The copyright holder for this preprint (which was not certified by peer review) is the author/funder, who has granted bioRxiv a license to display the preprint in perpetuity. It is made available under aCC-BY-NC-ND 4.0 International license.

819 al. Metalloproteinase inhibitors for the disintegrin-like metalloproteinases ADAM10 and
820 ADAM17 that differentially block constitutive and phorbol ester-inducible shedding of cell
821 surface molecules. Comb Chem High Throughput Screen. 2005;8(2):161-71. doi:
822 10.2174/1386207053258488. PubMed PMID: 15777180.
823 36. Black RA, Rauch CT, Kozlosky CJ, Peschon JJ, Slack JL, Wolfson MF, et al. A
824 metalloproteinase disintegrin that releases tumour-necrosis factor-alpha from cells. Nature.
825 1997;385(6618):729-33. doi: 10.1038/385729a0. PubMed PMID: 9034190.
826 37. Schlomann U, Koller G, Conrad C, Ferdous T, Golfi P, Garcia AM, et al. ADAM8 as
827 a drug target in pancreatic cancer. Nat Commun. 2015;6:6175. Epub 20150128. doi:
828 10.1038/ncomms7175. PubMed PMID: 25629724; PubMed Central PMCID:
829 PMCPMC5014123.
830 38. Tamura Y, Watanabe F, Nakatani T, Yasui K, Fuji M, Komurasaki T, et al. Highly
831 selective and orally active inhibitors of type IV collagenase (MMP-9 and MMP-2): N-
832 sulfonylamino acid derivatives. J Med Chem. 1998;41(4):640-9. doi: 10.1021/jm9707582.
833 PubMed PMID: 9484512.
834 39. Fray MJ, Dickinson RP, Huggins JP, Occleston NL. A potent, selective inhibitor of
835 matrix metalloproteinase-3 for the topical treatment of chronic dermal ulcers. J Med Chem.
836 2003;46(16):3514-25. doi: 10.1021/jm0308038. PubMed PMID: 12877590.

bioRxiv preprint doi: https://doi.org/10.1101/2021.12.14.472513; this version posted December 15, 2021. The copyright holder for this preprint (which was not certified by peer review) is the author/funder, who has granted bioRxiv a license to display the preprint in perpetuity. It is made available under aCC-BY-NC-ND 4.0 International license.

837 40. Levin JI, Chen J, Du M, Hogan M, Kincaid S, Nelson FC, et al. The discovery of
838 anthranilic acid-based MMP inhibitors. Part 2: SAR of the 5-position and P1(1) groups.
839 Bioorg Med Chem Lett. 2001;11(16):2189-92. doi: 10.1016/s0960-894x(01)00419-x. PubMed
840 PMID: 11514167.
841 41. Dales NA, Gould AE, Brown JA, Calderwood EF, Guan B, Minor CA, et al.
842 Substrate-based design of the first class of angiotensin-converting enzyme-related
843 carboxypeptidase (ACE2) inhibitors. J Am Chem Soc. 2002;124(40):11852-3. doi:
844 10.1021/ja0277226. PubMed PMID: 12358520.
845 42. Yeung ML, Teng JLL, Jia L, Zhang C, Huang C, Cai JP, et al. Soluble ACE2-
846 mediated cell entry of SARS-CoV-2 via interaction with proteins related to the renin-
847 angiotensin system. Cell. 2021;184(8):2212-28.e12. Epub 20210302. doi:
848 10.1016/j.cell.2021.02.053. PubMed PMID: 33713620; PubMed Central PMCID:
849 PMCPMC7923941.
850 43. Rodríguez E, Everitt E. Adenovirus uncoating and nuclear establishment are not
851 affected by weak base amines. J Virol. 1996;70(6):3470-7. doi: 10.1128/JVI.70.6.3470-
852 3477.1996. PubMed PMID: 8648679; PubMed Central PMCID: PMCPMC190220.
853 44. Zhang Z, Zheng Y, Niu Z, Zhang B, Wang C, Yao X, et al. SARS-CoV-2 spike protein
854 dictates syncytium-mediated lymphocyte elimination. Cell Death Differ. 2021;28(9):2765-77.

bioRxiv preprint doi: https://doi.org/10.1101/2021.12.14.472513; this version posted December 15, 2021. The copyright holder for this preprint (which was not certified by peer review) is the author/funder, who has granted bioRxiv a license to display the preprint in perpetuity. It is made available under aCC-BY-NC-ND 4.0 International license.

855 Epub 20210420. doi: 10.1038/s41418-021-00782-3. PubMed PMID: 33879858; PubMed
856 Central PMCID: PMCPMC8056997.
857 45. Bussani R, Schneider E, Zentilin L, Collesi C, Ali H, Braga L, et al. Persistence of
858 viral RNA, pneumocyte syncytia and thrombosis are hallmarks of advanced COVID-19
859 pathology. EBioMedicine. 2020;61:103104. Epub 20201103. doi: 10.1016/j.ebiom.2020.103104.
860 PubMed PMID: 33158808; PubMed Central PMCID: PMCPMC7677597.
861 46. Hoffmann M, Schroeder S, Kleine-Weber H, Müller MA, Drosten C, Pöhlmann S.
862 Nafamostat mesylate blocks activation of SARS-CoV-2: New treatment option for COVID-19.
863 Antimicrob Agents Chemother. 2020. Epub 2020/04/20. doi: 10.1128/AAC.00754-20. PubMed
864 PMID: 32312781.
865 47. Fan C, Lu W, Li K, Ding Y, Wang J. ACE2 Expression in Kidney and Testis May
866 Cause Kidney and Testis Infection in COVID-19 Patients. Front Med (Lausanne).
867 2020;7:563893. Epub 20210113. doi: 10.3389/fmed.2020.563893. PubMed PMID: 33521006;
868 PubMed Central PMCID: PMCPMC7838217.
869 48. Liu J, Li Y, Liu Q, Yao Q, Wang X, Zhang H, et al. SARS-CoV-2 cell tropism and
870 multiorgan infection. Cell Discov. 2021;7(1):17. Epub 20210323. doi: 10.1038/s41421-021-
871 00249-2. PubMed PMID: 33758165; PubMed Central PMCID: PMCPMC7987126.
872 49. Reis FM, Bouissou DR, Pereira VM, Camargos AF, dos Reis AM, Santos RA.

bioRxiv preprint doi: https://doi.org/10.1101/2021.12.14.472513; this version posted December 15, 2021. The copyright holder for this preprint (which was not certified by peer review) is the author/funder, who has granted bioRxiv a license to display the preprint in perpetuity. It is made available under aCC-BY-NC-ND 4.0 International license.

873 Angiotensin-(1-7), its receptor Mas, and the angiotensin-converting enzyme type 2 are
874 expressed in the human ovary. Fertil Steril. 2011;95(1):176-81. Epub 20100801. doi:
875 10.1016/j.fertnstert.2010.06.060. PubMed PMID: 20674894.
876 50. Jing Y, Run-Qian L, Hao-Ran W, Hao-Ran C, Ya-Bin L, Yang G, et al. Potential
877 influence of COVID-19/ACE2 on the female reproductive system. Mol Hum Reprod.
878 2020;26(6):367-73. doi: 10.1093/molehr/gaaa030. PubMed PMID: 32365180; PubMed Central
879 PMCID: PMCPMC7239105.
880 51. Henarejos-Castillo I, Sebastian-Leon P, Devesa-Peiro A, Pellicer A, Diaz-Gimeno P.
881 SARS-CoV-2 infection risk assessment in the endometrium: viral infection-related gene
882 expression across the menstrual cycle. Fertil Steril. 2020;114(2):223-32. Epub 20200617. doi:
883 10.1016/j.fertnstert.2020.06.026. PubMed PMID: 32641214; PubMed Central PMCID:
884 PMCPMC7298504.
885 52. Puelles VG, Lütgehetmann M, Lindenmeyer MT, Sperhake JP, Wong MN, Allweiss
886 L, et al. Multiorgan and Renal Tropism of SARS-CoV-2. N Engl J Med. 2020;383(6):590-2.
887 Epub 2020/05/13. doi: 10.1056/NEJMc2011400. PubMed PMID: 32402155; PubMed Central
888 PMCID: PMCPMC7240771.
889 53. Diao B, Wang C, Wang R, Feng Z, Zhang J, Yang H, et al. Human kidney is a target
890 for novel severe acute respiratory syndrome coronavirus 2 infection. Nat Commun.

bioRxiv preprint doi: https://doi.org/10.1101/2021.12.14.472513; this version posted December 15, 2021. The copyright holder for this preprint (which was not certified by peer review) is the author/funder, who has granted bioRxiv a license to display the preprint in perpetuity. It is made available under aCC-BY-NC-ND 4.0 International license.

2021;12(1):2506. Epub 20210504. doi: 10.1038/s41467-021-22781-1. PubMed PMID: 33947851; PubMed Central PMCID: PMCPMC8096808.

54. Johnson BA, Xie X, Bailey AL, Kalveram B, Lokugamage KG, Muruato A, et al. Loss of furin cleavage site attenuates SARS-CoV-2 pathogenesis. Nature. 2021;591(7849):293-9. Epub 20210125. doi: 10.1038/s41586-021-03237-4. PubMed PMID: 33494095; PubMed Central PMCID: PMCPMC8175039.

55. Peacock TP, Goldhill DH, Zhou J, Baillon L, Frise R, Swann OC, et al. The furin cleavage site in the SARS-CoV-2 spike protein is required for transmission in ferrets. Nat Microbiol. 2021;6(7):899-909. Epub 20210427. doi: 10.1038/s41564-021-00908-w. PubMed PMID: 33907312.

56. Benton DJ, Wrobel AG, Xu P, Roustan C, Martin SR, Rosenthal PB, et al. Receptor binding and priming of the spike protein of SARS-CoV-2 for membrane fusion. Nature. 2020;588(7837):327-30. Epub 20200917. doi: 10.1038/s41586-020-2772-0. PubMed PMID: 32942285; PubMed Central PMCID: PMCPMC7116727.

57. Stevens CS, Oguntuyo KY, Lee B. Proteases and variants: context matters for SARS-CoV-2 entry assays. Curr Opin Virol. 2021;50:49-58. Epub 20210724. doi: 10.1016/j.coviro.2021.07.004. PubMed PMID: 34365113; PubMed Central PMCID: PMCPMC8302850.

bioRxiv preprint doi: https://doi.org/10.1101/2021.12.14.472513; this version posted December 15, 2021. The copyright holder for this preprint (which was not certified by peer review) is the author/funder, who has granted bioRxiv a license to display the preprint in perpetuity. It is made available under aCC-BY-NC-ND 4.0 International license.

909 58. Harvey WT, Carabelli AM, Jackson B, Gupta RK, Thomson EC, Harrison EM, et al.
910 SARS-CoV-2 variants, spike mutations and immune escape. Nat Rev Microbiol.
911 2021;19(7):409-24. Epub 20210601. doi: 10.1038/s41579-021-00573-0. PubMed PMID:
912 34075212; PubMed Central PMCID: PMCPMC8167834.
913 59. The human protein atlas - Tissue expression of
914 ADAM10 https://www.proteinatlas.org/ENSG00000137845-ADAM10/tissue.
915 60. The human protein atlas - Cell type atlas
916 https://www.proteinatlas.org/ENSG00000137845-ADAM10/celltype.
917 61. Caescu CI, Jeschke GR, Turk BE. Active-site determinants of substrate recognition
918 by the metalloproteinases TACE and ADAM10. Biochem J. 2009;424(1):79-88. Epub
919 20091023. doi: 10.1042/BJ20090549. PubMed PMID: 19715556; PubMed Central PMCID:
920 PMCPMC2774824.
921 62. Carapito R, Li R, Helms J, Carapito C, Gujja S, Rolli V, et al. Identification of driver
922 genes for critical forms of COVID-19 in a deeply phenotyped young patient cohort. Sci Transl
923 Med. 2021:eabj7521. Epub 20211026. doi: 10.1126/scitranslmed.abj7521. PubMed PMID:
924 34698500.
925 63. Daniloski Z, Jordan TX, Wessels HH, Hoagland DA, Kasela S, Legut M, et al.
926 Identification of Required Host Factors for SARS-CoV-2 Infection in Human Cells. Cell.

bioRxiv preprint doi: https://doi.org/10.1101/2021.12.14.472513; this version posted December 15, 2021. The copyright holder for this preprint (which was not certified by peer review) is the author/funder, who has granted bioRxiv a license to display the preprint in perpetuity. It is made available under aCC-BY-NC-ND 4.0 International license.

927 2021;184(1):92-105.e16. Epub 20201024. doi: 10.1016/j.cell.2020.10.030. PubMed PMID:
928 33147445; PubMed Central PMCID: PMCPMC7584921.
929 64. Gunst JD, Staerke NB, Pahus MH, Kristensen LH, Bodilsen J, Lohse N, et al.
930 Efficacy of the TMPRSS2 inhibitor camostat mesilate in patients hospitalized with Covid-19-
931 a double-blind randomized controlled trial. EClinicalMedicine. 2021;35:100849. Epub
932 20210422. doi: 10.1016/j.eclinm.2021.100849. PubMed PMID: 33903855; PubMed Central
933 PMCID: PMCPMC8060682.
934 65. Boulware DR, Pullen MF, Bangdiwala AS, Pastick KA, Lofgren SM, Okafor EC, et
935 al. A Randomized Trial of Hydroxychloroquine as Postexposure Prophylaxis for Covid-19. N
936 Engl J Med. 2020;383(6):517-25. Epub 20200603. doi: 10.1056/NEJMoa2016638. PubMed
937 PMID: 32492293; PubMed Central PMCID: PMCPMC7289276.
938 66. Self WH, Semler MW, Leither LM, Casey JD, Angus DC, Brower RG, et al. Effect of
939 Hydroxychloroquine on Clinical Status at 14 Days in Hospitalized Patients With COVID-19:
940 A Randomized Clinical Trial. JAMA. 2020;324(21):2165-76. doi: 10.1001/jama.2020.22240.
941 PubMed PMID: 33165621; PubMed Central PMCID: PMCPMC7653542.
942 67. Matsuyama S, Nao N, Shirato K, Kawase M, Saito S, Takayama I, et al. Enhanced
943 isolation of SARS-CoV-2 by TMPRSS2-expressing cells. Proc Natl Acad Sci U S A.
944 2020;117(13):7001-3. Epub 2020/03/12. doi: 10.1073/pnas.2002589117. PubMed PMID:

bioRxiv preprint doi: https://doi.org/10.1101/2021.12.14.472513; this version posted December 15, 2021. The copyright holder for this preprint (which was not certified by peer review) is the author/funder, who has granted bioRxiv a license to display the preprint in perpetuity. It is made available under aCC-BY-NC-ND 4.0 International license.

945 32165541; PubMed Central PMCID: PMCPMC7132130.

946 68. Wang H, Li X, Nakane S, Liu S, Ishikawa H, Iwamoto A, et al. Co-expression of
947 foreign proteins tethered to HIV-1 envelope glycoprotein on the cell surface by introducing
948 an intervening second membrane-spanning domain. PLoS One. 2014;9(5):e96790. doi:
949 10.1371/journal.pone.0096790. PubMed PMID: 24804933; PubMed Central PMCID:
950 PMCPMC4013048.

951 69. Imai M, Iwatsuki-Horimoto K, Hatta M, Loeber S, Halfmann PJ, Nakajima N, et al.
952 Syrian hamsters as a small animal model for SARS-CoV-2 infection and countermeasure
953 development. Proc Natl Acad Sci U S A. 2020;117(28):16587-95. Epub 20200622. doi:
954 10.1073/pnas.2009799117. PubMed PMID: 32571934; PubMed Central PMCID:
955 PMCPMC7368255.

956 70. Yamamoto M, Abe C, Wakinaga S, Sakane K, Yumiketa Y, Taguchi Y, et al. TRAF6
957 maintains mammary stem cells and promotes pregnancy-induced mammary epithelial cell
958 expansion. Commun Biol. 2019;2:292. Epub 2019/08/06. doi: 10.1038/s42003-019-0547-7.
959 PubMed PMID: 31396572; PubMed Central PMCID: PMCPMC6684589.

960 71. Tani H, Shiokawa M, Kaname Y, Kambara H, Mori Y, Abe T, et al. Involvement of
961 ceramide in the propagation of Japanese encephalitis virus. J Virol. 2010;84(6):2798-807.
962 Epub 20100106. doi: 10.1128/JVI.02499-09. PubMed PMID: 20053738; PubMed Central

bioRxiv preprint doi: https://doi.org/10.1101/2021.12.14.472513; this version posted December 15, 2021. The copyright holder for this preprint (which was not certified by peer review) is the author/funder, who has granted bioRxiv a license to display the preprint in perpetuity. It is made available under aCC-BY-NC-ND 4.0 International license.

PMCID: PMCPMC2826033.

## Additional information

### Financial Disclosure Statement

This work was supported, in part, by the Platform Project for Supporting Drug Discovery and Life Science Research from the Japan Agency for Medical Research and Development (AMED) under Grant Number JP20am0101086 (support number 2834), and by grants-in-aid from the Ministry of Education, Culture, Sports, Science, and Technology, Japan (MEXT; 16H06575 to JI), from the Japanese Society for the Promotion of Science (JSPS; 15K21438 and 18K15235 to MY), from AMED [Program of Japan Initiative for Global Research Network on Infectious Diseases (JGRID) JP20wm0125002 to YK], and from the University of Tokyo (Promoting practical use of measures against coronavirus disease 2019 [COVID-19] to JI). The funders had no role in study design, data collection and analysis, decision to publish, or preparation of the manuscript.

**Competing interests:** The authors declare no competing interests.

bioRxiv preprint doi: https://doi.org/10.1101/2021.12.14.472513; this version posted December 15, 2021. The copyright holder for this preprint (which was not certified by peer review) is the author/funder, who has granted bioRxiv a license to display the preprint in perpetuity. It is made available under aCC-BY-NC-ND 4.0 International license.

## Figure Captions

**Fig 1. ACE2-dependent but TMPRSS2-independent membrane fusion activity of the SARS-CoV-2 S protein**

**(a)** Cell fusion kinetics induced by the S proteins from SARS-CoV, SARS-CoV-2, and MERS-CoV were determined using the DSP assay. Target cells expressing ACE2 alone or together with TMPRSS2 were used for co-culturing with effector cells expressing SARS-CoV S and SARS-CoV-2 S, and cells expressing CD26 alone or together with TMPRSS2 were used for co-culturing with effector cells expressing MERS-CoV- S. Relative cell-fusion values were calculated by normalizing the RL activity of each co-culture to that of the co-culture with cells expressing both receptor and TMPRSS2 at 240 min, which was set to 100%. Values are means ± SD ($n$ = 3/group). ** $p < 0.01$. (**b**) Phase contrast images of S protein-mediated cell fusion 16 h after co-culture. Red arrowheads indicate syncytia formation Scale bars, 100 μm. (**c**) Effect of nafamostat on the TMPRSS2-dependent cell fusion. Target cells expressing ACE2 with TMPRSS2 were used for co-culturing with effector cells expressing SARS-CoV S and SARS-CoV-2 S, and cells expressing CD26 with TMPRSS2 were used for co-culturing with effector cells expressing MERS-CoV- S. Relative cell-fusion values were calculated by normalizing the RL activity for each co-culture to that of the co-culture with cells expressing both

bioRxiv preprint doi: https://doi.org/10.1101/2021.12.14.472513; this version posted December 15, 2021. The copyright holder for this preprint (which was not certified by peer review) is the author/funder, who has granted bioRxiv a license to display the preprint in perpetuity. It is made available under aCC-BY-NC-ND 4.0 International license.

999 receptor and TMPRSS2 in the presence of DMSO, which was set to 100%. Values are
1000 means ± SD (*n* = 3/group). ** $p < 0.01$. (**d**) Effects of the nafamostat on the TMPRSS2-
1001 independent or -dependent cell fusion. Target cells expressing ACE2 alone or together
1002 with TMPRSS2 were used for co-culturing with effector cells expressing SARS-CoV-2
1003 S. Relative cell-fusion value was calculated by normalizing the RL activity for each co-
1004 culture to that of the co-culture with cells expressing both ACE2 and TMPRSS2 in the
1005 presence of DMSO, which was set to 100%. Values are means ± SD (*n* = 3/group). nafamo,
1006 nafamostat.
1007
1008 **Fig 2. TMPRSS2-independent membrane fusion induced by the S protein of SARS-**
1009 **CoV-2 is blocked by various metalloproteinase inhibitors.**
1010 **(a)** High-throughput screening of the Validated Compound Library (1,630 clinically
1011 approved compounds and 1,885 pharmacologically active compounds) in the DSP assay
1012 using the SARS-CoV-2 S protein. The x-axis shows the relative cell-fusion value using
1013 cells expressing both TMPRSS2 and ACE2 in the presence of each compound (1 μM in
1014 DMSO), n = 1. The y-axis shows the relative cell-fusion value using cells expressing
1015 ACE2 alone in the presence of each compound (1 μM in DMSO), n = 1. The relative cell-
1016 fusion value was calculated by normalizing the RL activity for each compound to that of

bioRxiv preprint doi: https://doi.org/10.1101/2021.12.14.472513; this version posted December 15, 2021. The copyright holder for this preprint (which was not certified by peer review) is the author/funder, who has granted bioRxiv a license to display the preprint in perpetuity. It is made available under aCC-BY-NC-ND 4.0 International license.

the control assay (DMSO alone; set to 100%). Each dot represents an individual compound. Dots in the red-dashed box indicate compounds that preferentially inhibit TMPRSS2-independent membrane fusion. (< 30% inhibition of the relative cell fusion value using the target cells expressing both TMPRSS2 and ACE2 and > 40% inhibition of the relative cell-fusion value using the target cells expressing ACE2 alone. The compound names for the candidates are indicated. (**b**) Effects of the metalloproteinase inhibitors on cell fusion in the co-cultures of the cells expressing SARS-CoV-2 S protein with those expressing ACE2 alone or in combination with TMPRSS2. Relative cell-fusion values were calculated by normalizing the RL activity for each co-culture to that of the co-culture with cells expressing both ACE2 and TMPRSS2 in the presence of DMSO, which was set to 100%. Values are means ± SD ($n$ = 3/group). ** $p < 0.01$.

**Fig 3. The metalloproteinase-dependent viral entry pathway is cell type-dependent.** Effects of drugs on the entry of SARS-CoV-2 S-bearing vesicular stomatitis virus (VSV) pseudotype virus. The relative pseudovirus entry was calculated by normalizing the FL activity for each condition to the FL activity of cells infected with SARS-CoV-2 S-bearing pseudovirus in the presence of DMSO alone, which was set to 100%. Values are means ± SD ($n$ = 3/group). * $p < 0.05$, ** $p < 0.01$. Cont: cells infected with pseudovirus

bioRxiv preprint doi: https://doi.org/10.1101/2021.12.14.472513; this version posted December 15, 2021. The copyright holder for this preprint (which was not certified by peer review) is the author/funder, who has granted bioRxiv a license to display the preprint in perpetuity. It is made available under aCC-BY-NC-ND 4.0 International license.

without S protein; SARS-CoV-2: cells infected with SARS-CoV-2 S-bearing pseudovirus. E-64d: 25 μM E-64d, nafamo: 10 μM nafamostat, marima: 1 μM marimastat. (**a**) Effects of marimastat, E-64d, or nafamostat on the pseudovirus entry in A704, OVISE, and Calu-3 cells, respectively. (**b-e**) Effects of a single drug treatment or a combination treatment on the pseudovirus entry in VeroE6, HEC50B, OVTOKO and A704 cells (b), IGROV1, OUMS-23 and OVISE cells (c), Calu-3 and Caco-2 (d), and HEC50B-TMPRSS2 cells (e).

**Fig 4. The metalloproteinase-dependent entry pathway requires both the furin-cleavage site and S2 region of the SARS-CoV-2 S protein.**

Effects of drugs on the entry of S protein-bearing vesicular stomatitis virus (VSV) pseudotype virus. The relative pseudovirus entry was calculated by normalizing the FL activity for each condition to the FL activity of cells infected with pseudovirus in the presence of DMSO alone, which was set to 100%. Values are means ± SD ($n$ = 3/group). ** $p < 0.01$. Cont: cells infected with pseudovirus without S protein. E-64d: 25 μM E-64d, marima: 1 μM marimastat, nafamo: 10 μM nafamostat. (**a**) Effects of E-64d and marimastat on the entry of pseudoviruses bearing SARS-CoV S, SARS-CoV-2 S, MERS-CoV S, or VSV G in HEC50B cells. **b**, Effects of E-64d and marimastat on the entry of

bioRxiv preprint doi: https://doi.org/10.1101/2021.12.14.472513; this version posted December 15, 2021. The copyright holder for this preprint (which was not certified by peer review) is the author/funder, who has granted bioRxiv a license to display the preprint in perpetuity. It is made available under aCC-BY-NC-ND 4.0 International license.

HCoV-NL63 S and WIV1-CoV S pseudovirus in HEC50B cells. **c**, Schematic illustration of C-terminally Flag-tagged chimeric S proteins in which the S1, S1/S2 boundary, and S2 domain from SARS-CoV S (red) or SARS-CoV-2 S (yellow) are indicated (top). Amino acid sequences of the residues around the S1/S2 boundary of the coronaviruses (bottom). Numbers refer to the amino acid residues. F: Flag-tag. Arginine residues in the S1/S2 cleavage site and furin cleavage motif are highlighted in red. (**d**) Expression of chimeric S protein in pseudoviruses. S proteins were detected using an anti-Flag-tag antibody that binds to a Flag-tag on the C-terminus of the S proteins (top). Detection of the vesicular stomatitis virus matrix protein (VSV M) served as the control (bottom). S0: uncleaved S protein; S2: cleaved S2 domain of the S protein. (**e, f**) Effects of E-64d and marimastat on the entry of pseudoviruses bearing chimeric S proteins in HEC50B cells. (**g**) Effects of E-64d and nafamostat on the entry of pseudoviruses bearing SARS-CoV S, SARS-CoV-2 S, MERS-CoV S, or VSV G in HEC50B-TMPRSS2 cells in the presence of marimastat. (**h, i**) Effects of E-64d and nafamostat on the entry of pseudoviruses bearing chimeric S proteins in HEC50B-TMPRSS2 cells in the presence of marimastat.

**Fig 5. Possible involvement of ADAM-10 in the metalloproteinase-dependent entry of SARS-CoV-2.**

bioRxiv preprint doi: https://doi.org/10.1101/2021.12.14.472513; this version posted December 15, 2021. The copyright holder for this preprint (which was not certified by peer review) is the author/funder, who has granted bioRxiv a license to display the preprint in perpetuity. It is made available under aCC-BY-NC-ND 4.0 International license.

**(a)** Effects of metalloprotease inhibitors on the entry of pseudoviruses bearing SARS-CoV-2 S or VSV G in VeroE6 and HEC50B cells in the presence of E-64d, and A704 cells in the absence of E-64d. The relative pseudovirus entry was calculated by normalizing the FL activity for each condition to the FL activity of cells infected with pseudovirus in the presence of DMSO alone, which was set to 100%. Values are means ± SD (*n* = 3/group). Data were compared with those obtained from cells infected pseudoviruses bearing SARS-CoV-2 S in the presence of E-64d for HEC50B and VeroE6, and in the presence of DMSO alone for A704. * $p < 0.05$, ** $p < 0.01$. Cont: cells infected with pseudovirus without S protein. marima: marimastat, prinoma: prinomastat, iloma: ilomastat, CTS: CTS-1027, UK: UK370106, GW: GW280264X, GI: GI254023X, MLN: MLN-4760, BK: BK-1361, MMP2/9i: MMP2/9 inhibitor I, MMP9i: MMP9 inhibitor I. (**b**) Effects of the ADAM10 knockdown on ACE2 (top), ADAM10 (middle), and tubulin (bottom) expression. HEC50B cells were transfected with two distinct control siRNAs or three distinct siRNAs against Adam10 for 48 h. (**c**) The effect of the ADAM10 knockdown on the entry of pseudoviruses bearing SARS-CoV-2 S, SARS-CoV S, MERS-CoV S, or VSV G. HEC50B cells were transfected with siRNAs for 48 h and then infected with pseudoviruses. The relative pseudovirus entry was calculated by normalizing the FL activity for each condition to the FL activity of cells infected with

bioRxiv preprint doi: https://doi.org/10.1101/2021.12.14.472513; this version posted December 15, 2021. The copyright holder for this preprint (which was not certified by peer review) is the author/funder, who has granted bioRxiv a license to display the preprint in perpetuity. It is made available under aCC-BY-NC-ND 4.0 International license.

pseudovirus in the absence of siRNA (mock), which was set to 100%. Values are means ± SD (*n* = 3/group). * $p < 0.05$, ** $p < 0.01$. (**d, e**) Effect of ADAM10 knockdown on the patterns of the entry pathways for SARS-CoV-2 S pseudovirus in HEC50B cells. HEC50B cells were transfected with siRNAs for 48 h and then infected with pseudoviruses in the presence of drugs. Values are means ± SD (*n* = 3/group). ** $p < 0.01$. E-64d: 25 μM E-64d, marima: 1 μM marimastat. Data are displayed as the conditions of siRNA treatment (d) and drug treatment (e).

**Fig 6. The metalloproteinase-dependent entry pathway of authentic SARS-CoV-2 is involved in syncytia formation and cytopathicity.**

Effects of the drugs on the cytoplasmic viral RNA after SARS-CoV-2 infection. The relative amount of viral RNA in the cells was normalized to cellular *Rpl13a* mRNA expression. Values are means ± SD (*n* = 3/group in a-d, *n* = 10/group in e). * $p < 0.05$, ** $p < 0.01$. (**a**) Effects of marimastat or prinomastat on SARS-CoV-2 infection in HEC50B, A704, and VeroE6 cells. (**b**) Effects of marimastat and the inhibitor of the endosome pathway on SARS-CoV-2 infection in HEC50B, A704, and VeroE6 cells. marima: 1 μM marimastat, E-64d: 25 μM E-64d, NH4Cl: 10 mM NH4Cl. (**c**) Effect of marimastat, E-64d, and nafamostat on SARS-CoV-2 infection in HEC50B-TMPRSS2 cells. marima: 1

bioRxiv preprint doi: https://doi.org/10.1101/2021.12.14.472513; this version posted December 15, 2021. The copyright holder for this preprint (which was not certified by peer review) is the author/funder, who has granted bioRxiv a license to display the preprint in perpetuity. It is made available under aCC-BY-NC-ND 4.0 International license.

μM marimastat, E-64d: 25 μM E-64d, nafamo: 10 μM nafamostat. (**d**) Effects of selective metalloprotease inhibitors on SARS-CoV-2 infection in HEC50B cells. GW: GW280264X, GI: GI254023X. (**e**) Effect of ADAM10 knockdown on SARS-CoV-2 infection in HEC50B cells. (**f, g**) Effects of drugs on SARS-CoV-2-induced syncytia formation in HEC50B (f) and HEC50B-TMPRSS2 (g) cells. Cells were stained with anti-SARS-CoV-2 N antibody (green) 24 h after infection. Nuclei were stained with Hoechst 33342 (blue). Scale bars, 200 μm. (**h, i**) Effects of drugs on SARS-CoV-2-induced cytopathicity in HEC50B (h) and HEC50B-TMPRSS2 (i) cells. marima: marimastat, prinoma: prinomastat. E-64d: 25 μM E-64d, nafamo: 10 μM nafamostat. Values are means ± SD (*n* = 3/group). ** $p < 0.01$.

## Supporting information

**S1 Fig. Cell-based membrane-fusion assay for coronavirus S proteins using the DSP reporter.**

(**a**) A method to monitor cell-cell membrane fusion mediated by the S protein of coronaviruses[24, 25]. Effector cells (293FT cells expressing DSP8-11 and S protein) and target cells (293FT cells expressing DSP1-7 and receptor protein with TMPRSS2 for "cell fusion with TMPRSS2" (top) or receptor protein without TMPRSS2 for "cell fusion

bioRxiv preprint doi: https://doi.org/10.1101/2021.12.14.472513; this version posted December 15, 2021. The copyright holder for this preprint (which was not certified by peer review) is the author/funder, who has granted bioRxiv a license to display the preprint in perpetuity. It is made available under aCC-BY-NC-ND 4.0 International license.

without TMPRSS2" (bottom)) were co-cultured for 4 h. Both GFP (fluorescence) and RL (luminescence) signals were generated following DSP1-7 and DSP8-11 reassociation upon mixing of the cells during the assay. (**b**) Expression of S proteins in effector cells were detected using an anti-Flag-tag antibody that binds to a Flag-tag on the C-terminus of S proteins (top). Tubulin was used as a control (bottom panel). S0: uncleaved S protein; S2: cleaved S2 domain of the S protein. (**c**) Schematic diagram of split chimeric reporter proteins. DSP1-7 has the structure RL1–155-Ser-Gly-Gly-Gly-Gly-GFP1–156. DSP8-11 has the Met- GFP157–231 -Gly-Gly-Gly-Gly-Ser- RL156–311. As GFP1–156 contains the first seven β sheets, and GFP157–231 contains the remaining four β sheets, the split proteins were called DSP1-7 and DSP8-11, respectively. DSP1-7 and DSP8-11 reassociate efficiently, resulting in the reconstitution of functional RL and GFP to generate luminescent and fluorescent signals, respectively.

**S2 Fig. Control experiments for the DSP assay.**

**(a**) A method to check whether compounds directly inhibit DSP activity without affecting cell-cell fusion[25]. 293FT cells expressing DSP1-7 and DSP8-11 were treated with compounds for 4 h. Measuring RL activities of the preformed DSP1-7/DSP8-11 complex to check whether the compounds directly inhibit RL activities without affecting cell-cell

bioRxiv preprint doi: https://doi.org/10.1101/2021.12.14.472513; this version posted December 15, 2021. The copyright holder for this preprint (which was not certified by peer review) is the author/funder, who has granted bioRxiv a license to display the preprint in perpetuity. It is made available under aCC-BY-NC-ND 4.0 International license.

fusion. (**b**) Effect of metalloproteinase inhibitors on RL activity. Relative DSP activity was calculated by normalizing the RL activity for each condition to that of the control assay (DMSO alone; set to 100%). Values are means ± SD (*n* = 3/group).

**S3 Fig. Effects of candidate compounds on the cell-cell fusion and RL activities.**

Effector cells expressing SARS-CoV-2 S were co-cultured with target cells expressing ACE2 alone for the TMPRSS2-independent cell-cell fusion assay (blue) or cells expressing ACE2 with TMPRSS2 for the TMPRSS2-dependent cell-cell fusion assay (red) in the presence of candidate compounds for 4 h. Cells expressing DSP1-7 and DSP8-11 in the presence of candidate compounds for 4 h to determine whether compounds directly inhibit RL activities (purple). Relative DSP activity was calculated by normalizing the RL activity for each condition to that of the control assay (DMSO alone; set to 100%). Values are means ± SD (*n* = 3/group).

**S4 Fig. The metalloproteinase-dependent entry pathway strictly requires both the furin-cleavage site and S2 region of S protein of SARS-CoV-2.**

Effects of the drugs on the entry of S protein-bearing vesicular stomatitis virus (VSV) pseudotype virus. The relative pseudovirus entry was calculated by normalizing the FL

bioRxiv preprint doi: https://doi.org/10.1101/2021.12.14.472513; this version posted December 15, 2021. The copyright holder for this preprint (which was not certified by peer review) is the author/funder, who has granted bioRxiv a license to display the preprint in perpetuity. It is made available under aCC-BY-NC-ND 4.0 International license.

activity for each condition to the FL activity of the cells infected with pseudovirus in the presence of DMSO alone, which was set to 100%. Values are means ± SD (*n* = 3/group). ** $p < 0.01$. Cont: cells infected with pseudovirus without S protein. E-64d: 25 μM E-64d, marima: 1 μM marimastat, nafamo: 10 μM nafamostat. (**a, b**) Effects of E-64d and marimastat on the entry of pseudoviruses bearing SARS-CoV S, SARS-CoV-2 S, MERS-CoV S, or VSV G in A704 (a) and VeroE6 (b) cells. (**c, d**) Effects of E-64d and marimastat on the entry of pseudoviruses bearing chimeric S proteins in VeroE6 cells. (**e**) Effects of E-64d and nafamostat on the entry of pseudoviruses bearing SARS-CoV S, SARS-CoV-2 S, MERS-CoV S, or VSV G in VeroE6-TMPRSS2 cells. (**f, g**) Effects of E-64d and nafamostat on the entry of pseudoviruses bearing chimeric S proteins in VeroE6-TMPRSS2 cells. To establish VeroE6 cells expressing TMPRSS2 (VeroE6-TMPRSS2), recombinant pseudotype lentivirus expressing TMPRSS2 was produced using 293T cells with a VSV-G-expressing plasmid. Cells infected with pseudotype viruses were selected with 300 μg/mL hygromycin for at least 1 week.

**S5 Fig. Patterns of entry pathways were conserved in various variants of SARS-CoV-2.**

bioRxiv preprint doi: https://doi.org/10.1101/2021.12.14.472513; this version posted December 15, 2021. The copyright holder for this preprint (which was not certified by peer review) is the author/funder, who has granted bioRxiv a license to display the preprint in perpetuity. It is made available under aCC-BY-NC-ND 4.0 International license.

**(a**) Expression of WT or mutant SARS-CoV-2 S proteins with mutations precent in B.1.1.7, B.1.351, B.1.617.1 and B.1.617.2 variants in the pseudoviruses. S proteins were detected using an anti-Flag-tag antibody that binds to a Flag-tag on the C-terminus of S proteins (top). Detection of vesicular stomatitis virus matrix protein (VSV M) served as a control (bottom). S0: uncleaved S protein; S2: cleaved S2 domain of the S protein. (**b**) Effects of E-64d and marimastat on the entry of pseudoviruses bearing SARS-CoV-2 S in VeroE6 cells. E-64d: 25 μM E-64d, marima: 1 μM marimastat. (**c**) Effects of nafamostat on the entry of pseudovirus bearing SARS-CoV-2 S in VeroE6-TMPRSS2 cells. (**d**) Effects of E-64d and marimastat on the entry of pseudoviruses bearing SARS-CoV-2 S in HEC50B cells. E-64d: 25 μM E-64d, marima: 1 μM marimastat. (**e**) Effects of marimastat on the entry of pseudoviruses bearing SARS-CoV-2 S in A704 cells. (**f**) Effects of nafamostat on the entry of pseudoviruses bearing SARS-CoV-2 S in Calu-3 cells. The relative pseudovirus entry was calculated by normalizing the FL activity for each condition to the FL activity of cells infected with pseudovirus in the presence of DMSO alone, which was set to 100%. Values are means ± SD (*n* = 3/group in b-f). Data were compared with those obtained from cells infected pseudoviruses bearing variant SARS-CoV-2 S in the presence of DMSO alone. * $p < 0.05$, ** $p < 0.01$. Cont: cells infected with a pseudovirus without S protein in (**b-f**).

bioRxiv preprint doi: https://doi.org/10.1101/2021.12.14.472513; this version posted December 15, 2021. The copyright holder for this preprint (which was not certified by peer review) is the author/funder, who has granted bioRxiv a license to display the preprint in perpetuity. It is made available under aCC-BY-NC-ND 4.0 International license.

**S6 Fig. Expression of WIV1-CoV and HCoV-NL63 S protein in pseudoviruses.**

**(a**) Schematic illustration of C-terminally FLAG-tagged S proteins of WIV1-CoV and HCoV-NL63 and amino acid sequences of the residues around the S1/S2 boundary of the coronaviruses (bottom). Numbers refer to amino acid residues. F: Flag tag. Arginine residues in the S1/S2 cleavage site and furin cleavage motif are highlighted in red. (**b**) Expression of S protein in pseudoviruses S proteins were detected using an anti-Flag-tag antibody that binds to a Flag-tag on the C-terminus of S proteins (top). The detection of VSV M served as a control (bottom). S0: uncleaved S protein; S2: cleaved S2 domain of the S protein.

**S7 Fig. Effects of drugs on cell viabilities.**

**(a-c)** VeroE6 (a), HEC50B (b), and A704 (c) cells were treated with various drugs, and cell viability was analyzed using Celltiter-Glo 24 h after the treatment. The relative cell viability was calculated by normalizing the FL activity for each condition to the FL activity of the cells in the presence of DMSO alone, which was set to 100%. Values are means ± SD (*n* = 3/group). (**d, e**) HEC50B (d), and HEC50B-TMPRSS2 (e) cells were treated with various drugs for 3 days. Half of the culture supernatant was replaced daily

bioRxiv preprint doi: https://doi.org/10.1101/2021.12.14.472513; this version posted December 15, 2021. The copyright holder for this preprint (which was not certified by peer review) is the author/funder, who has granted bioRxiv a license to display the preprint in perpetuity. It is made available under aCC-BY-NC-ND 4.0 International license.

with fresh medium containing the drugs. The relative cell viability was calculated by normalizing the FL activity for each condition to the FL activity of cells in the presence of DMSO alone, which was set to 100%. Values are means ± SD (*n* = 6/group).

**S8 Fig. Patterns of the entry pathways of the pseudovirus bearing SARS-CoV-2 S were not affected by the ADAM17 knockout in the HEC50B cells.**

(**a**) Effect of the ADAM17 knockout on ACE2 (top), ADAM17 (middle), and tubulin (bottom). (**b**) Effect of the ADAM17 knockout on the entry of the pseudoviruses bearing SARS-CoV-2 S. Values are means ± SD (*n* = 3/group). ** $p < 0.01$. (**c**) Effect of the ADAM17 knockout on the patterns of the entry pathways of SARS-CoV-2 S pseudovirus in HEC50B cells. The relative pseudovirus entry was calculated by normalizing the FL activity for each condition to the FL activity of cells infected with pseudovirus in the presence of DMSO alone, which was set to 100%. Values are means ± SD (*n* = 3/group). * $p < 0.05$, ** $p < 0.01$. E-64d: 25 μM E-64d, marima: 1 μM marimastat. To establish the ADAM17-knockout HEC50B cells, lentiviruses were produced by transfecting the lentiCRISPRv2 vector (#52961 Addgene, MA, USA) with the following gRNA sequences. The gRNA sequences used were 5′-GCG AGG TAT TCG GCT CCG CG-3’ (Cont #1), 5′-GCT TTC ACG GAG GTT CGA CG-3’ (Cont #2) and 5′-ATG TTG CAG

bioRxiv preprint doi: https://doi.org/10.1101/2021.12.14.472513; this version posted December 15, 2021. The copyright holder for this preprint (which was not certified by peer review) is the author/funder, who has granted bioRxiv a license to display the preprint in perpetuity. It is made available under aCC-BY-NC-ND 4.0 International license.

TTC GGC TCG AT-3' (Cont #3) for the control experiments, and 5′-AAC GTT CAG TAC TTG ATG TC-3' (ADAM10 #1) and 5′-GGA CTT CTT CAC TGG ACA CG-3' (ADAM10 #2) and 5′-CTT AAG GTG AGC CTG ACT CT-3' (ADAM10 #3) for the establishment of ADAM17-knockout cells. Pooled HEC50B cells infected with pseudotype viruses were selected with 1 μg/mL puromycin for 1 week.

**S9 Fig. Effects of drugs on SARS-CoV-2 infection.**

**(a**) Effects of the nafamostat on the SARS-CoV-2 infection in Calu-3, HEC50B, A704, and VeroE6 cells. Values are means ± SD (*n* = 3/group). ** $p < 0.01$. (**b**) Effects of the E-64d on the SARS-CoV-2 infection in HEC50B, A704, and VeroE6 cells. Values are means ± SD (*n* = 3/group). * $p < 0.05$, ** $p < 0.01$. (**c**) Effects of the $NH_4Cl$ on the SARS-CoV-2 infection in HEC50B cells. Values are means (*n* = 2/group). The relative amount of viral RNA in the cells was normalized to cellular *Rpl13a* mRNA expression in (a-c).

**S10 Fig. The metalloproteinase-dependent entry pathway of authentic SARS-CoV-2 is involved in syncytia formation.**

Phase contrast images of syncytia formation 24 h after SARS-CoV-2 infection in the presence of inhibitors. Red arrowheads indicate syncytia formation Scale bars, 100 μm.

bioRxiv preprint doi: https://doi.org/10.1101/2021.12.14.472513; this version posted December 15, 2021. The copyright holder for this preprint (which was not certified by peer review) is the author/funder, who has granted bioRxiv a license to display the preprint in perpetuity. It is made available under aCC-BY-NC-ND 4.0 International license.

1250

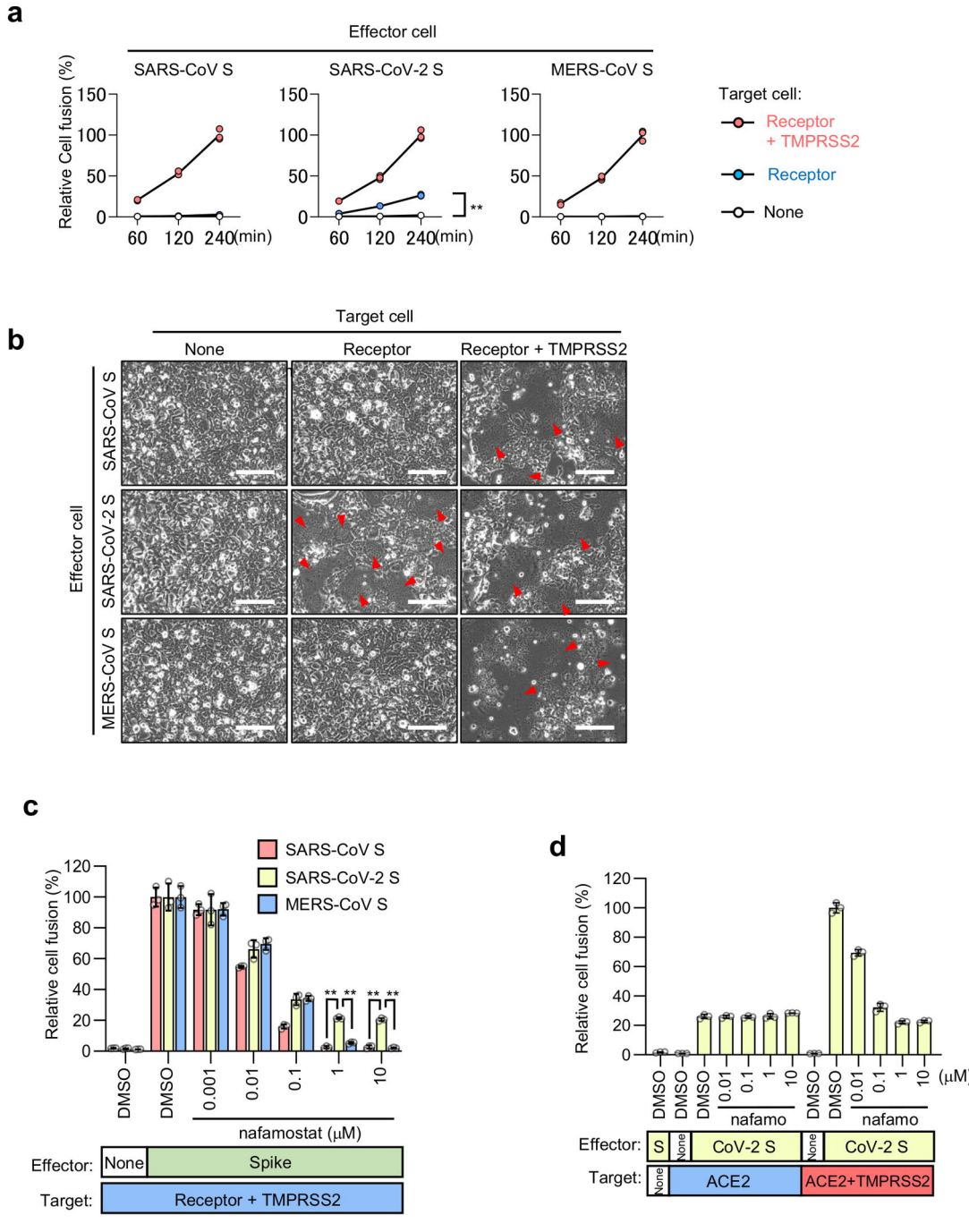
a
Effector cell
SARS-CoV S
SARS-CoV-2 S
MERS-CoV S
Relative Cell fusion (%)
150
100
50
0
60 120 240(min)
**
Target cell:
Receptor + TMPRSS2
Receptor
None
b
Target cell
None
Receptor
Receptor + TMPRSS2
Effector cell
SARS-CoV S
SARS-CoV-2 S
MERS-CoV S
c
SARS-CoV S
SARS-CoV-2 S
MERS-CoV S
Relative cell fusion (%)
120
100
80
60
40
20
0
**
DMSO
DMSO
0.001
0.01
0.1
1
10
nafamostat (μM)
Effector:
None
Spike
Target:
Receptor + TMPRSS2
d
Relative cell fusion (%)
120
100
80
60
40
20
0
DMSO
DMSO
DMSO
0.01
0.1
1
10
DMSO
DMSO
0.01
0.1
1
10
(μM)
nafamo
nafamo
Effector:
S
None
CoV-2 S
None
CoV-2 S
Target:
None
ACE2
ACE2+TMPRSS2

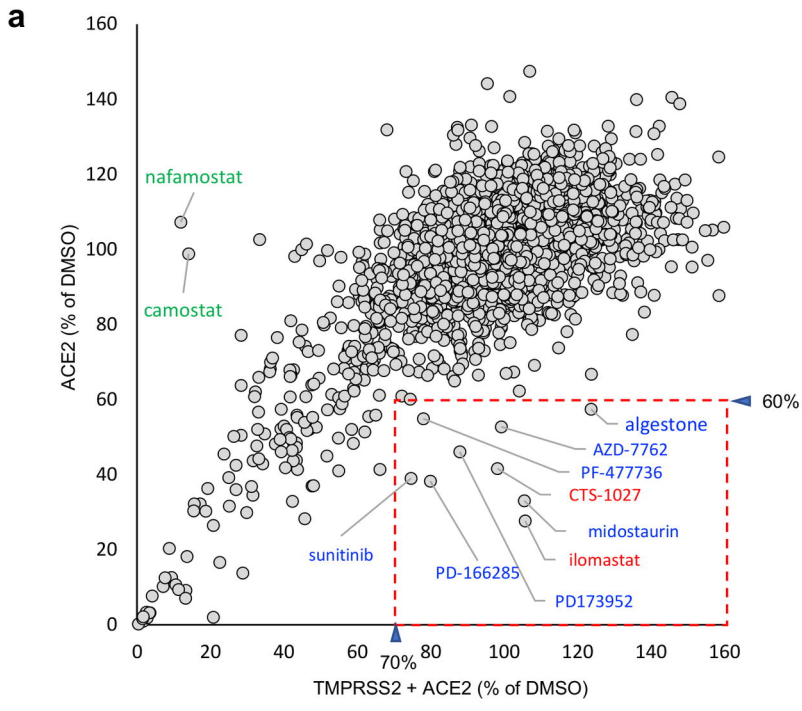
a
ACE2 (% of DMSO)
TMPRSS2 + ACE2 (% of DMSO)
nafamostat
camostat
algestone
AZD-7762
PF-477736
CTS-1027
midostaurin
ilomastat
PD173952
PD-166285
sunitinib
60%
70%

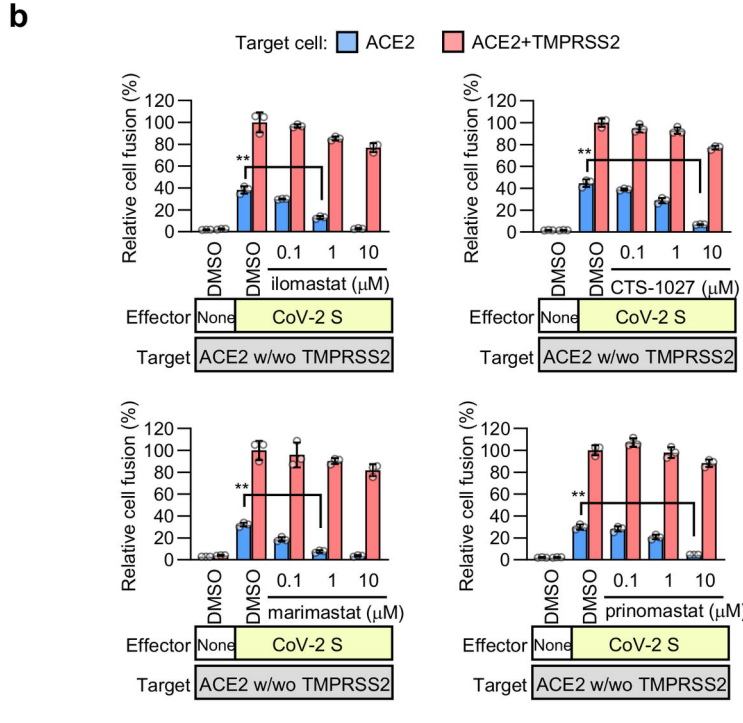
b
Target cell: ACE2 ACE2+TMPRSS2
Relative cell fusion (%)
DMSO
0.1
1
10
ilomastat (μM)
CTS-1027 (μM)
marimastat (μM)
prinomastat (μM)
Effector
None
CoV-2 S
Target
ACE2 w/wo TMPRSS2

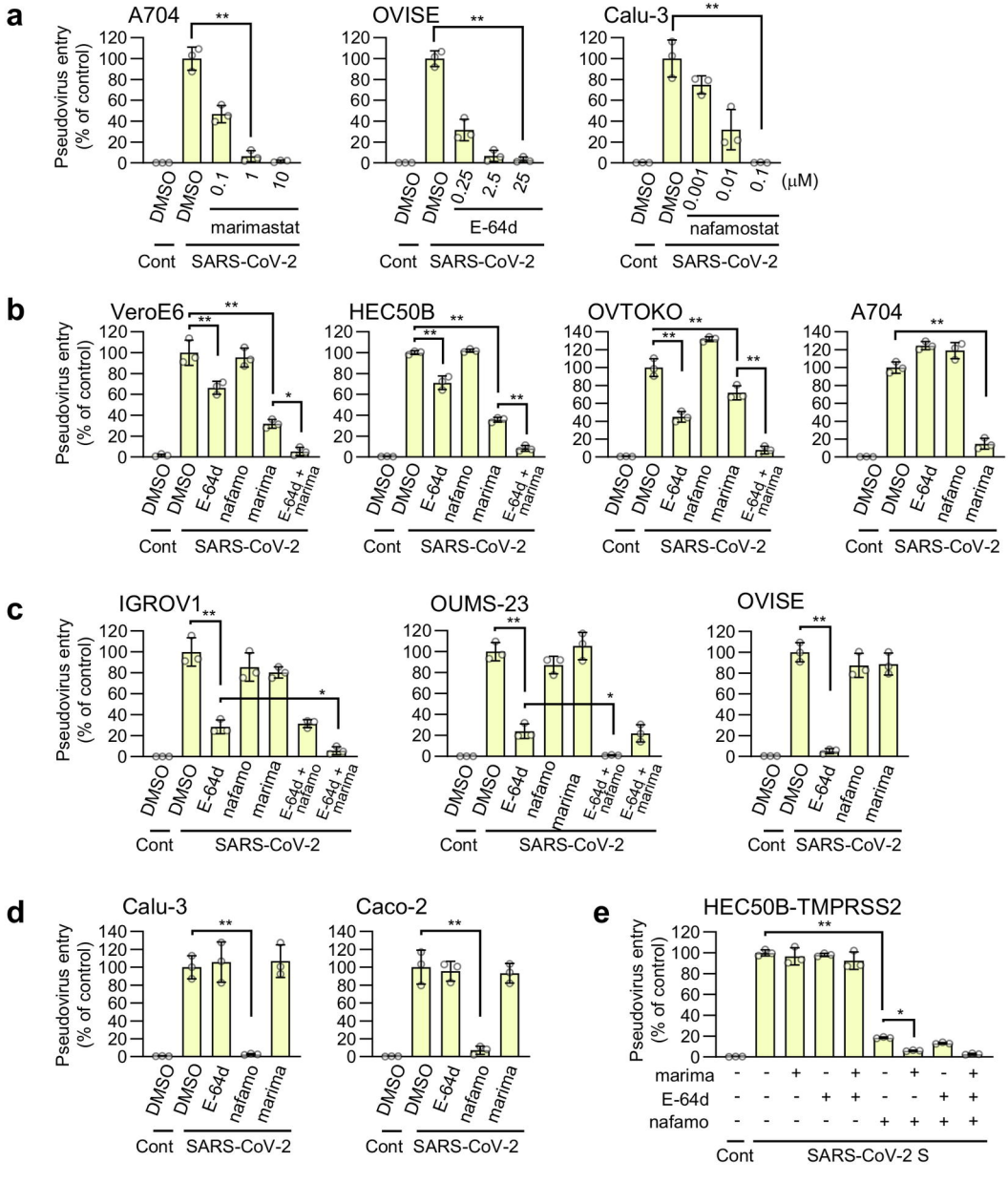
a
A704
OVISE
Calu-3
Pseudovirus entry (% of control)
DMSO
0.1
1
10
marimastat
0.25
2.5
25
E-64d
0.001
0.01
0.1
(μM)
nafamostat
Cont
SARS-CoV-2
b
VeroE6
HEC50B
OVTOKO
A704
E-64d
nafamo
marima
E-64d + marima
c
IGROV1
OUMS-23
OVISE
E-64d + nafamo
d
Calu-3
Caco-2
e
HEC50B-TMPRSS2
marima
E-64d
nafamo
SARS-CoV-2 S

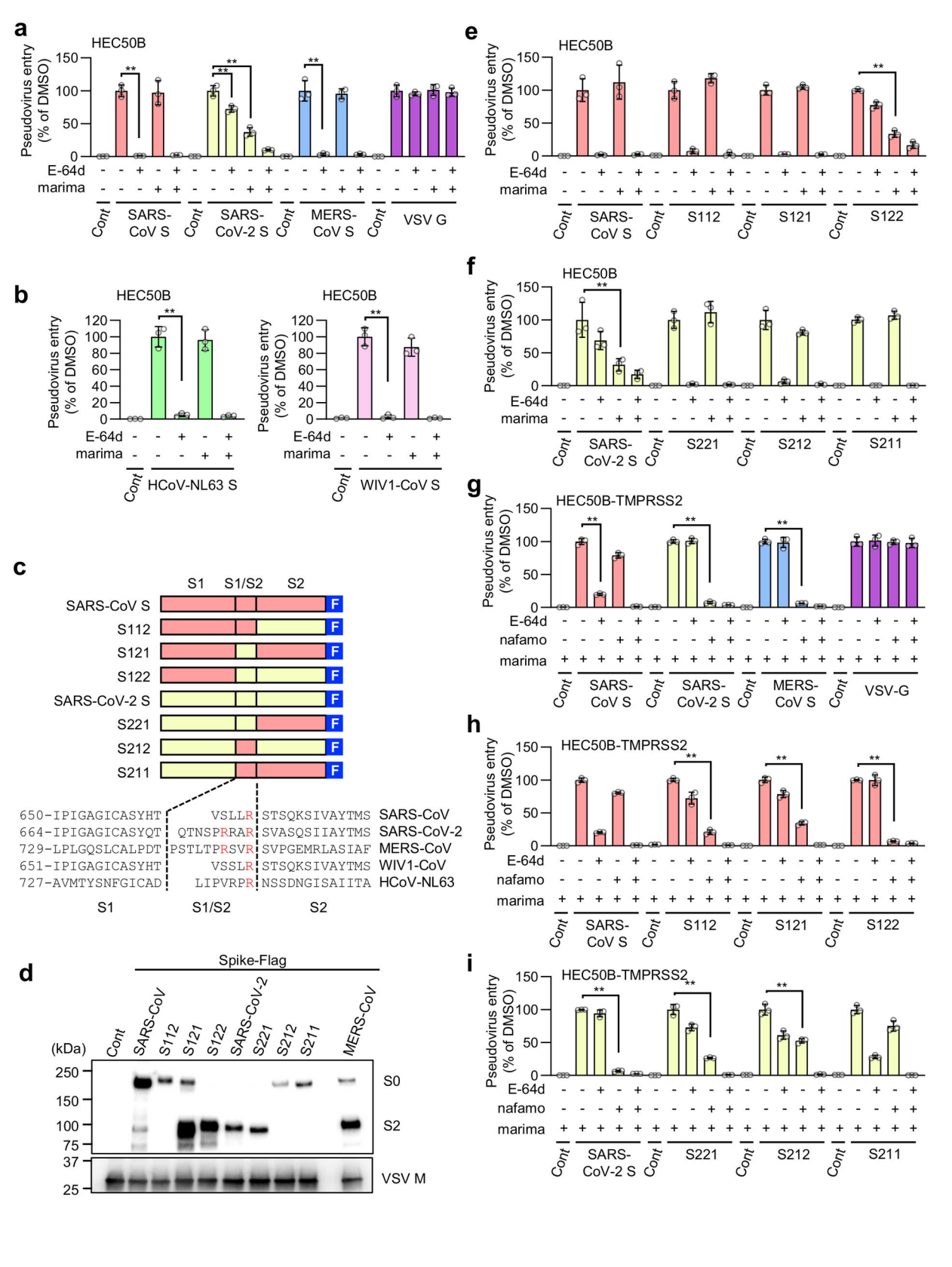
a
HEC50B
Pseudovirus entry (% of DMSO)
E-64d
marima
Cont
SARS-CoV S
SARS-CoV-2 S
MERS-CoV S
VSV G
b
HEC50B
HCoV-NL63 S
WIV1-CoV S
c
S1
S1/S2
S2
SARS-CoV S
S112
S121
S122
SARS-CoV-2 S
S221
S212
S211
650-IPIGAGICASYHT VSLLR STSQKSIVAYTMS SARS-CoV
664-IPIGAGICASYQT QTNSPRRAR SVASQSIIAYTMS SARS-CoV-2
729-LPLGQSLCALPDT PSTLTPRSVR SVPGEMRLASIAF MERS-CoV
651-IPIGAGICASYHT VSSLR STSQKSIVAYTMS WIV1-CoV
727-AVMTYSNFGICAD LIPVRPR NSSDNGISAIITA HCoV-NL63
d
Spike-Flag
(kDa)
S0
S2
VSV M
e
f
g
HEC50B-TMPRSS2
nafamo
h
i

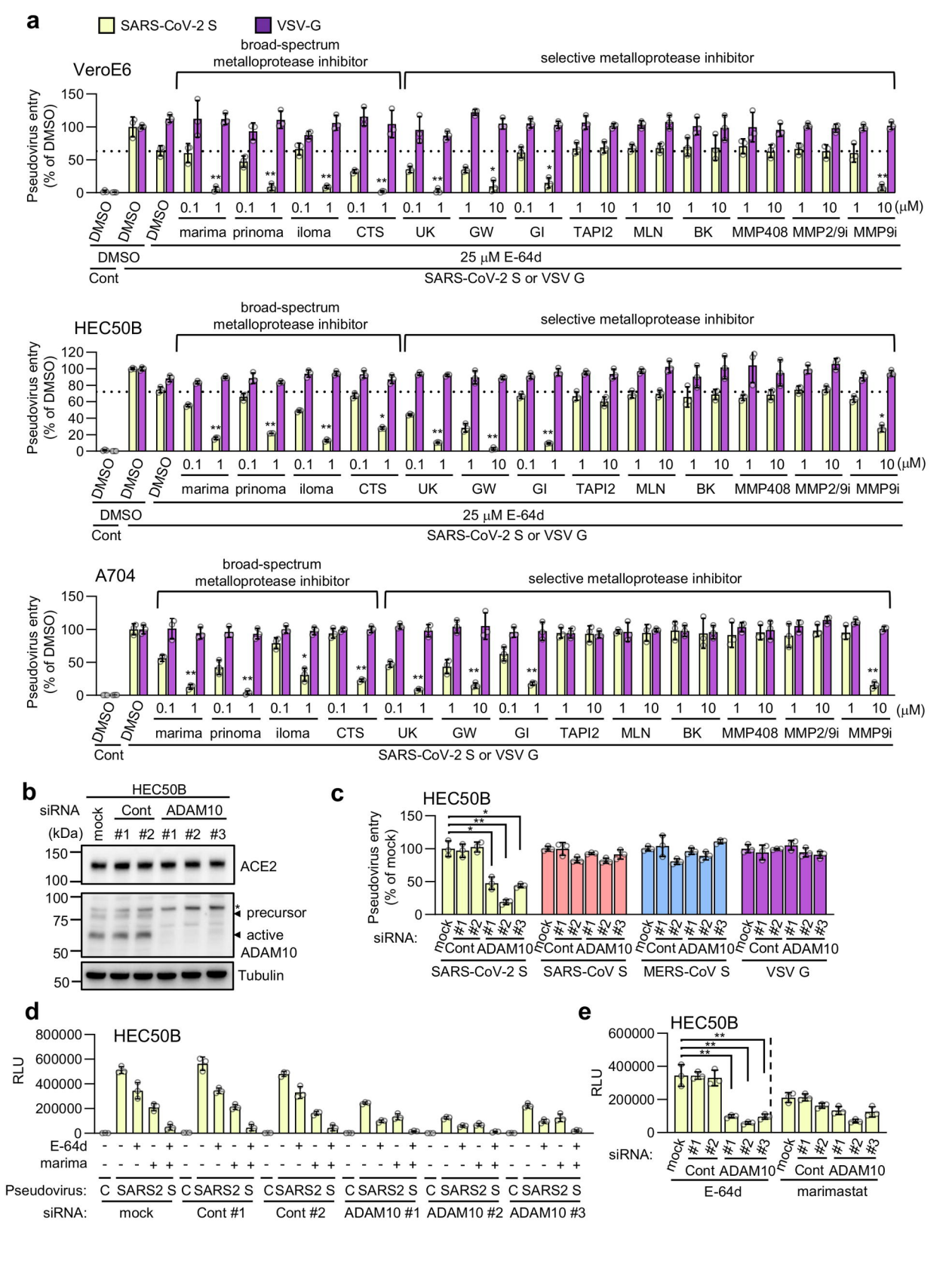
a
SARS-CoV-2 S
VSV-G
VeroE6
broad-spectrum metalloprotease inhibitor
selective metalloprotease inhibitor
Pseudovirus entry (% of DMSO)
DMSO
marima
prinoma
iloma
CTS
UK
GW
GI
TAPI2
MLN
BK
MMP408
MMP2/9i
MMP9i
(μM)
25 μM E-64d
Cont
SARS-CoV-2 S or VSV G
HEC50B
A704
b
HEC50B
siRNA
mock
Cont
ADAM10
(kDa)
ACE2
precursor
active ADAM10
Tubulin
c
HEC50B
Pseudovirus entry (% of mock)
siRNA:
SARS-CoV-2 S
SARS-CoV S
MERS-CoV S
VSV G
d
HEC50B
RLU
E-64d
marima
Pseudovirus:
C
SARS2 S
siRNA:
mock
Cont #1
Cont #2
ADAM10 #1
ADAM10 #2
ADAM10 #3
e
HEC50B
RLU
siRNA:
E-64d
marimastat

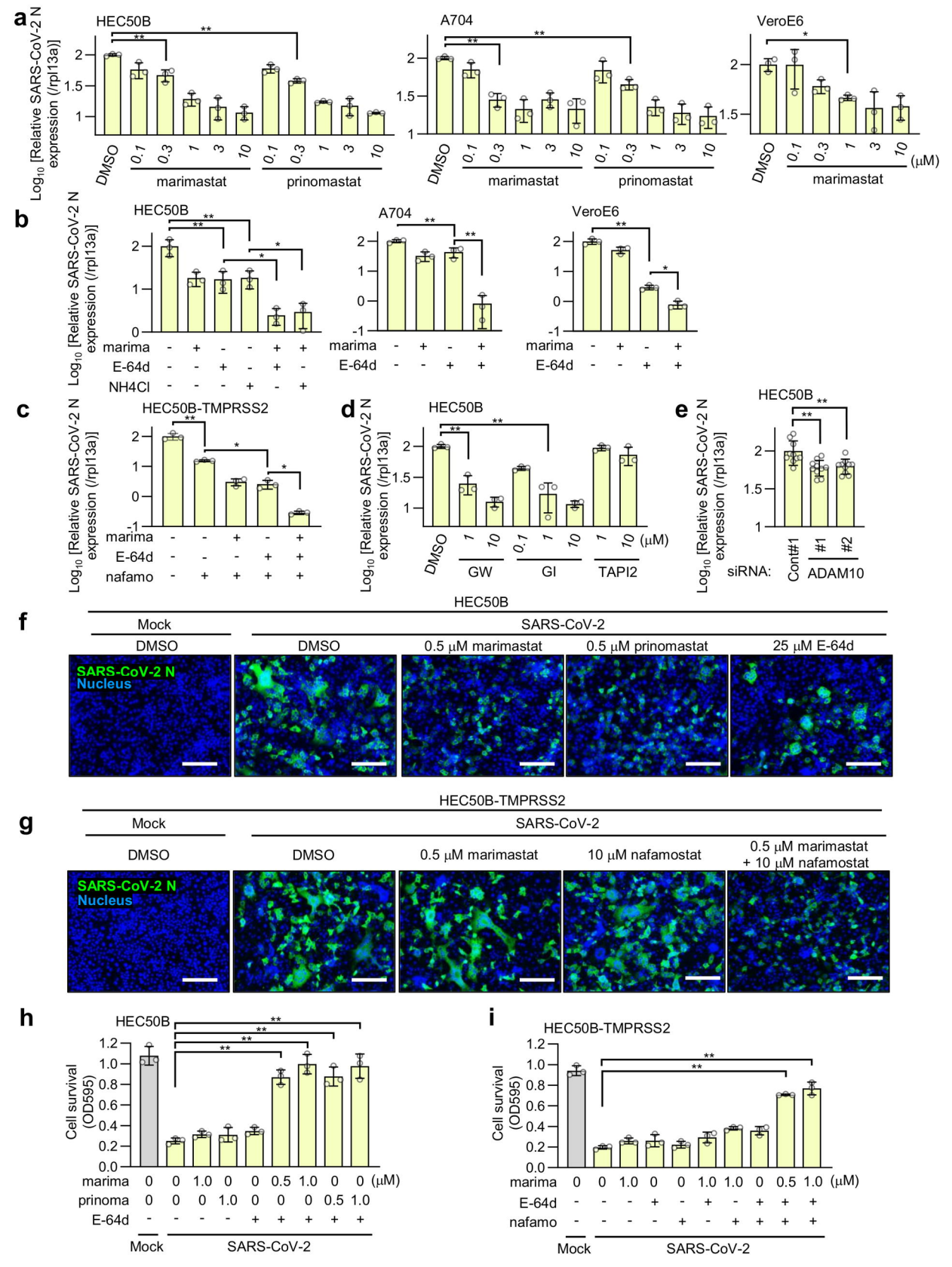
a
HEC50B
A704
VeroE6
Log10 [Relative SARS-CoV-2 N expression (/rpl13a)]
DMSO
0.1
0.3
1
3
10
marimastat
prinomastat
(μM)
b
HEC50B
A704
VeroE6
marima
E-64d
NH4Cl
c
HEC50B-TMPRSS2
nafamo
d
HEC50B
GW
GI
TAPI2
e
HEC50B
siRNA:
Cont#1
#1
#2
ADAM10
f
HEC50B
Mock
SARS-CoV-2
DMSO
0.5 μM marimastat
0.5 μM prinomastat
25 μM E-64d
SARS-CoV-2 N
Nucleus
g
HEC50B-TMPRSS2
10 μM nafamostat
0.5 μM marimastat + 10 μM nafamostat
h
HEC50B
Cell survival (OD595)
prinoma
i
HEC50B-TMPRSS2